

Unravelling the origins and P-T-t evolution of the allochthonous Sobrado unit (Órdenes Complex, NW Iberia) using combined U-Pb titanite, monazite and zircon geochronology and REE geochemistry

José Manuel Benítez-Pérez^{1,3}, Pedro Castiñeiras², Juan Gómez-Barreiro^{3(*)}, José Ramón Martínez Catalán³, Andrew Kylander-Clark⁴, Robert Holdsworth⁵

¹Centro de Ciências e Tecnologias Nucleares. Instituto Superior Técnico. Universidad de Lisboa. Estrada Nacional 10 (km 139,7), 2695-066, Bobadela LRS, Portugal

²Departamento de Mineralogía y Petrología. Facultad de Ciencias Geológicas, Universidad Complutense de Madrid. C/ José Antonio Novais, 12. Ciudad Universitaria, 28040, Madrid, Spain

³Departamento de Geología, Universidad de Salamanca, Pza. de los Caídos s/n, 37008, Salamanca, Spain

⁴Department of Earth Science, University of California, Santa Barbara, CA 93106, United States

⁵Earth Science Department, Durham University, Science Labs, Durham DH1 3LE, United Kingdom

Correspondence to: J. Gómez Barreiro (jugb@usal.es)

jose.benitez@ctn.tecnico.ulisboa.pt

castigar@ucm.es

kylander@geol.ucsb.edu

r.e.holdsworth@durham.ac.uk

Abstract

The Sobrado unit, within the upper part of the Ordenes complex (NW Iberia) represents an allochthonous tectonic slice of exhumed high grade metamorphic rocks formed during a complex sequence of orogenic processes in the middle to lower crust. In order to constrain those processes, U-Pb geochronology and REE analyses of accessory minerals in migmatitic paragneisses (monazite, zircon), and mylonitic amphibolites (titanite) were conducted using LASS-ICP-MS. The youngest metamorphic zircon age obtained co-incides with a Middle Devonian concordia monazite age (~380 Ma) and is interpreted to represent the minimum age of the Sobrado high-P granulite-facies metamorphism that occurred during the early stages of the Variscan Orogeny. Metamorphic titanites from the mylonitic amphibolites yield a Late Devonian age (~365 Ma) and track the progressive exhumation of the Sobrado unit. In zircon, cathodoluminescence images and REE analyses allow two aliquots with different origins in the paragneiss to be distinguished. An Early Ordovician age (~490 Ma) was obtained for metamorphic zircons, although with a large dispersion, related to the evolution of the rock. This age is considered to mark the onset of granulite-facies metamorphism in the Sobrado unit under intermediate-P conditions, and related to intrusive magmatism and coeval burial in a magmatic arc setting. A maximum depositional age for the Sobrado unit is established in the late Cambrian (~511 Ma). The zircon dataset also record several inherited populations. The youngest cogenetic set of zircons yield crystallization ages of 546 and 526 Ma and are thought to be related to the peri-Gondwana magmatic arc. The additional presence of inherited zircons older than 1000 Ma is interpreted as suggesting a West African Craton provenance.

Keywords: U-Pb geochronology, LASS-ICP, zircon, titanite, monazite, REE, Sobrado Unit

1. Introduction

1 Zircon, monazite and titanite are accessory mineral phases found in rocks with a very wide range
2 of compositions. These minerals can resist numerous sedimentary, igneous and metamorphic events
3 across a wide range of temperatures, pressures and strains, even when fluids are present. Frequently,
4 compositional domains can be defined in these minerals that record changes in different parameters
5 (Storey et al., 2007; Castiñeiras et al., 2010; Stübner et al., 2014; Hacker et al., 2015; Stearns et al., 2016;
6 Stipska et al., 2016). These minerals additionally provide several closed decay chains or disintegration
7 systems ($^{238}\text{U} \rightarrow ^{206}\text{Pb}$, $^{235}\text{U} \rightarrow ^{207}\text{Pb}$ y $^{232}\text{Th} \rightarrow ^{208}\text{Pb}$), because they hold variable concentrations of
8 uranium (U) and/or thorium (Th) in their crystal lattices. Such variations in concentration allow accurate
9 dating using microscopic scale analysis (tens of microns size).

10 Titanite is stable in metabasites across a wide range of metamorphic conditions (Spear, 1981;
11 Frost et al., 2000) and is able to record metamorphic and deformational events (Franz and Spear, 1985;
12 Verts and Frost, 1996; Rubatto and Hermann, 2001; Spencer et al., 2013; Stearns et al., 2015, 2016). The
13 titanite U/Pb system is a widely used geochronometer for deformation events in granulite-amphibolite
14 facies rocks (Spear, 1981; Cherniak, 2006; Harlov et al., 2006). Monazite is common in amphibolite and
15 higher-grade facies. Zoning in this mineral can have an igneous or metamorphic origin (DeWolf et al.,
16 1993; Hawkins and Bowring, 1997; Zhu et al., 1997; Spear and Pyle, 2002). The crystallization stages
17 seen in zoned monazites, with changes in Y, Ca, Si, Sr, Ba, REE, U and Th, has been linked to certain
18 metamorphic reactions (Kohn and Malloy, 2004; Corrie and Kohn, 2008) or deformation process (Terry
19 and Hamilton, 2000). Zircon survives the majority of magmatic, metamorphic and erosive terrestrial
20 processes. Cathodoluminescence analysis of zircon zoning patterns allows a large variety of reactions to
21 be distinguished and can clarify the petrogenetic evolution (Corfu et al., 2003). Th/U ratios can also be
22 used to separate zircon based on their igneous or metamorphic origin (Hoskin and Ireland, 2000; Möller
23 et al., 2002; Hokada and Harley, 2004; Hoskin, 2005). Rare-earth element (REE) abundances can also be
24 used as a qualitative petrological indicator. Heavy rare-earth elements (HREE) are preferentially
25 incorporated into zircon compared to light rare-earth elements (LREE). Hence, the normalized HREE
26 slope can be used to interpret whether a zircon crystallized or recrystallized when garnet and xenotime
27 (YPO_4) were present, because these minerals also preferentially assimilate HREE in the lattice (Hoskin
28 and Ireland, 2000; Rubatto, 2002; Hermann and Rubatto, 2003; Rubatto et al., 2009).

29 The events recorded in individual grains can be radiometrically dated employing combined laser
30 ablation analyses and cathodoluminescence (CL) images in zircons (Corfu et al., 2003) and compositional
31 maps obtained using electron microprobe (EMPA) in monazite (Gonçalves et al., 2005; Williams et al.,
32 2007) to recognize different growth zones. The chemical analysis, especially REE, links the development
33 of growth zones to specific metamorphic or deformative events (Frost et al., 2000; Rubatto, 2002;
34 Whitehouse and Platt, 2003; Zheng et al., 2007; Chen et al., 2010; Gagnevin and Daly, 2010; Holder et
35 al., 2015;). Simultaneous geochronology and REE data are a powerful tool in the interpretation of ages -
36 this is known as REE-assisted geochronology (Castiñeiras et al., 2010).

37 In the present study, monazite and zircon ages of paragneisses and titanite ages of amphibolites
38 taken from separate, but presently adjacent tectonic slices of the high-P/high-T of Sobrado unit are
39 compared and interpreted using REE-assisted geochronology. This sheds new light upon the possible
40 origin, ages and relationships between the regional foliation development and the partial melting
41 processes that have occurred in the Sobrado unit.

42 43 **2. Geological background**

44 The Allochthonous complexes in NW Iberia are remnants of a huge nappe stack preserved as
45 klippen in the core of late Variscan synforms. They consist of units mostly of peri-Gondwanan derivation,
46 which can be classified in three groups based on their structural position in the tectonic pile and origin:
47 The Upper, Middle and Lower allochthons.

1 The Upper Allochthon is a piece of the northern margin of Gondwana detached and drifted away
2 during the Cambro-Ordovician opening of the Rheic Ocean. The Middle Allochthon is formed by
3 lithospheric pieces of oceanic affinity, or oceanic supracrustal sequences that formed part of the Rheic
4 oceanic realm and are often referred to as ophiolitic units. The Lower Allochthon derives from distal parts
5 of the Gondwanan continental margin.

6 The Allochthon units are separated from the Iberian Autochthon by a series of kilometer-scale
7 imbricated sheets, known as the Parautochthon (Ribeiro et al., 1990), or Schistose Domain in Galicia
8 (NW Spain), consisting of a set of Paleozoic metasedimentary and volcanic rocks. The Parautochthon has
9 stratigraphic and igneous affinities with the Iberian autochthon of the Central Iberian Zone, and no
10 ophiolites occur between them. For these reasons it is interpreted as a distal part of the Gondwanan
11 continental margin (Farias et al., 1987; Dias da Silva et al., 2014).

12 The allochthonous units are regarded as a stack of Varican thrust sheets with associated tectonic
13 fabrics and metamorphic events. Due to the "piggy-back" nature of the sequence, the structurally higher
14 units are thought to represent the furthest travelled paleogeographic domains. Recumbent folds, thrusts
15 and extensional detachments formed during the Variscan collision are found in all three allochthonous
16 units (Martínez Catalán et al., 1999; Gómez-Barreiro et al., 2007).

17 Maximum sedimentation ages obtained from the study of **isotopic zircon** carried out in
18 metasediments from the Upper allochthon can be estimated between 530 and 510 Ma (e.g., Fuenlabrada
19 et al., 2010). Intrusive rocks in the Upper allochthon have been **dated between 520 and 490 Ma** and are
20 associated with the development of **a magmatic arc and extension of crust** (Peucat et al., 1990; Ordóñez
21 Casado, 1998; Abati et al., 1999, 2007; Fernández-Suárez et al., 2007; Castiñeiras et al., 2010). Two
22 high-P/high-T metamorphic events have been recognized in this unit. **The oldest one has yielded 490-480**
23 **Ma (Kuijper 1979; Peucat et al. 1990; Abati et al., 1999, 2007; Fernández-Suárez et al., 2002) and the**
24 **youngest one has been dated approximately between 405-390 Ma (Santos Zalduegui et al., 1996; Ordóñez**
25 **Casado et al., 2001; Fernández-Suárez et al., 2007).** In the Middle allochthon, crystallization ages vary
26 between **390 and 375 Ma** (Peucat et al., 1990; Dallmeyer et al., 1991, 1997) and ages from **375 to 365 Ma**
27 have been related to continental subduction (Santos Zalduegui et al., 1995; Abati et al., 2010). Thrust
28 wedge collapse, in the middle and lower allochthonous units, is thought to have happened between 390
29 and 365 Ma, followed by a collision in the internal zones around 365-330 Ma, causing further folding and
30 thrusts (Dallmeyer et al., 1997; Martínez Catalán et al., 2009). Afterwards, there was another extensional
31 collapse phase until 315 Ma, followed by a final phase of shortening and folding up until approximately
32 305 Ma related to the regional oroclinal bending in Iberia (Aerden, 2004; Martínez Catalán, 2011, 2012;
33 Álvarez-Valero et al., 2014).

34 The Upper Allochthon is further subdivided into high-P/high-T and intermediate-P units (Gómez
35 Barreiro et al., 2007). The present study focuses on two of **the high-P/high T upper** units. The origin of
36 the high-P event recorded in these units is controversial, but might reflect the accretion of the units into
37 the continental part of northern Gondwana, during the Early-Middle Devonian (400-390 Ma; Ballèvre et
38 al., 2014).

39 **The Sobrado antiform consists of three tectonic slices bounded by two extensional detachments**
40 **(Fig 1).** The lower horse comprises highly serpentinized ultramafic rocks with interlayered metabasite
41 units. The metabasites include eclogites (Omp + Grt + Qtz + Rt ± Ky and Zo, mineral abbreviations
42 according to Kretz, 1983) and related clinopyroxene-garnet rocks without primary plagioclase (Na-Di +
43 Grt + Qtz + Rt ± Zo), as well as other types of rocks derived from the retrogression and mylonitization of
44 the early high-P stages. The intermediate slice is made up of migmatitic felsic gneisses (mainly
45 paragneisses), with frequent inclusions of high-P granulites (Na-Di + Grt + Pl + Qtz + Rt ± Ky). **Relicts**
46 of igneous protoliths are not preserved either in the lower or intermediate slices. The upper slice,
47 however, contains migmatitic felsic gneisses and mafic layers derived from deformed and recrystallized
48 gabbros with locally preserved relict igneous textures, reaching high-P granulite facies conditions. The

1 progressive transformation from gabbros to high-P granulites (Na-Di + Grt + Pl + Qtz + Rt) has occurred
2 in a series of different stages with a metamorphic peak at 13-17 kbar and 660-770°C (Arenas and
3 Martínez Catalán, 2002).

4 The metamorphic evolution described by most authors in the Sobrado Unit suggests that felsic
5 gneisses underwent differing degrees of partial melting after the metabasites reached their peak pressure.
6 Consequently, the felsic gneisses are thought to have developed a regional foliation under amphibolite
7 facies conditions, as did the amphibolic gneisses, "flaser" amphibolites, and fine-grained amphibolites.
8 This metamorphic evolution is described by Arenas and Martínez Catalán (2002) as a clockwise P-T path,
9 with a metamorphic peak of, at least, 15 kbar and >800°C, followed by a strongly isothermal and
10 decompressive trajectory. This trajectory is interpreted to result from gravitational collapse of an
11 overthickened orogenic wedge (Gómez-Barreiro et al., 2007; Ballèvre et al., 2014). Although some
12 regional structures, such as the Fornás detachment (Gómez-Barreiro et al., 2007; Álvarez-Valero et al.,
13 2014) or the Corredoiras detachment (Díaz García et al., 1998) have been related to this gravitational
14 readjustment, no study has dealt with the development of these fabrics in any detail. Overall, it is thought
15 that the extensional flow has generated a pervasive thinning of the orogenic pile and that the preserved
16 sequence of tectonic slices is strongly condensed.

17 3. Methodology

18 3.1. Selected samples

19 Two samples (*JBP-71-15A* and *JBP-71-21*) were selected from two structurally separate but
20 currently adjacent parts of the high-P/high-T Sobrado unit, within the Órdenes complex, for laser ablation
21 (LASS-Laser Ablation Split Stream) analyses, including U–Pb geochronology and REE determinations.
22 The sample locations are presented in Figure 1. Sample *JBP-71-21* is a mylonitic fine-grained
23 amphibolite, without any preserved igneous relicts. It is located at the base of the upper tectonic slice and
24 comprises Hbl + Pl + Grt ± Cpx + Bt + Rt ± Ttn ± Ilm. Sample *JBP-71-15A* is a granulite facies
25 migmatitic paragneiss from the underlying intermediate tectonic slice. It comprises Qtz + Pl + Grt + Kfs
26 + Ky + Bt + Ilm + Rt and shows microscopic scale textural evidence of partial melting.

27 3.2. Sample preparation

28 Sample preparation was carried out at the laboratories of the Universidad Complutense (Madrid).
29 The rocks were crushed, pulverized and sieved to achieve a 0.1-0.5 mm grain size. Heavy minerals were
30 concentrated using a Wilfley™ table. The non-magnetic minerals from this heavy fraction is then
31 separated using a Frantz isodynamic magnetic separator. A final concentrated fraction is obtained using
32 heavy liquids (methylene iodide, CH₂I₂).

33 Zircon (translucent, colourless or light brown), monazite (yellow) and titanite (colorless) grains
34 are selected by handpicking, according to their external morphology viewed under a binocular
35 microscope. All the grains collected were arranged separately in parallel rows, mounted on glass slide
36 with a double-sided adhesive and set in epoxy resin. After the resin was cured, the surface was eroded
37 using a wet abrasive silicon carbide abrasive paper (4000 grit) and polished with 0.3 μm aluminium
38 oxide. The surface was then coated with gold, to avoid charging problems under the scanning electron
39 microscope (SEM). Prior to isotopic analysis, cathodoluminescence images (CL) of zircon grains were
40 taken on a JEOL JSM-820 SEM, and compositional maps of monazite grains were created on a JEOL
41 Superprobe JXA-8900M microprobe (National Center for Electron Microscopy, Madrid). Secondary
42 electron images (SE) were also taken to determine the exact location of the spots, identify the internal
43 structure, and presence of inclusions and defects in zircon, monazite and titanite grains.

44 3.3. Mineral description

45 Titanite grains are generally rounded, with an average grain size of 100 μm, and irregular
46 morphologies. Their secondary electron images reveal homogeneous compositions and the presence of
47 solid inclusions. This grain size permits large spatial resolution analyses (50 μm) to be carried out.

1 Monazite grains have a more variable grain size distribution, with an average of 60-70 μm . Their habit is
2 irregular and they usually show rounded morphologies or broken grains. We carried out La, Th, Y, U and
3 Nd compositional maps for every monazite grain in order to discover a compositional zonation that could
4 be attributed to different growth events. Thorium zoning is the one that developed better and was taken
5 into account to select the spots for isotopic analysis (Fig. 4), yet it never exceeds 30% of the grain.
6 Several spots were analyzed in monazite crystals with the greatest compositional contrasts to determine if
7 they really represented different growth stages in the monazite grains.

8 Zircon grains from the paragneisses usually have scarce mineral inclusions and they can display
9 a wide variety of morphologies, including irregular and sub-rounded shapes typical of metamorphic
10 zircon, pristine elongated dipyrarnidal prisms interpreted as igneous in origin, and equigranular grains
11 with abrasion signs with a probable detrital origin. Their length-to-width ratios vary between 3:1 and 2:1.
12 Cathodoluminescence images (Fig. 2) are useful to relate the crystallization of parts of zircon crystals to
13 specific igneous, metamorphic or deformational events (Corfu et al., 2003, Nasdala et al., 2003, Zeck et
14 al., 2004). It is common to image a homogeneous xenocrystic core in zircon grains and even a less
15 luminescent mantle in some grains (grain numbers 5, 6). The core aspect is mainly rounded, with
16 irregular or angular shapes. In most of the zircon grains, the internal parts of the grains display an
17 oscillatory zoning (grain numbers 33, 71), with different thickness, although in some cases, this zoning is
18 faint (grain number 26). There are several grains with sector zones (grain numbers 26, 27) parallel to the
19 zircon *c*-axis (Watson and Yan Liang, 1995) and even one case of soccerball zoning (grain number 82).
20 The zoning usually appears to be partially truncated and surrounded by a discontinuous poorly
21 luminescent rim (grain numbers 20, 79).

22 3.4. Analytical techniques

23 U/Th-Pb, REE and Hf analyses of zircon, titanite and monazite were carried out using the laser
24 ablation split stream (LASS) at the University of California at Santa Barbara (UCSB). The samples were
25 ablated using a Photon Machines 193 nm ArF excimer ultraviolet laser with a HelEx ablation cell coupled
26 to a Nu Instruments Plasma high-resolution multi-collector inductively coupled plasma mass
27 spectrometer (MC-ICP-MS) and either a Nu Instruments AttoM high-resolution single-collector ICP or
28 an Agilent 7700S quadrupole ICP-MS (Kylander-Clark et al., 2013). This installation allows the
29 simultaneous isotopic and compositional (REE) analysis to be carried out. The laser spot diameter was 20
30 μm for zircon, 7-10 μm for monazite (Kořler et al., 2001) and 50 μm for titanite (Stearns et al., 2016),
31 resulting in pit depths between 6 μm for monazite and 30 μm for titanite. The laser has a fluence of ~ 1
32 J/cm^2 , and was fired twice to remove common Pb from the sample surface and this material was allowed
33 to wash out for 15 s, prior to the material being ablated at 3 Hz for 20 s. On the ICP-MS, the masses
34 $^{204}\text{Pb}+\text{Hg}$, ^{206}Pb , ^{207}Pb , and ^{208}Pb were measured using ion counters, and the masses ^{232}Th and ^{238}U were
35 measured using Faraday detectors.

36 The U/Th-Pb standardization for monazite was carried out using sample 44069 (Aleinikoff et al.,
37 2006) as the primary reference material (RM), whereas the Bananeira sample was employed as primary
38 RM for trace element corrections (Kylander-Clark et al., 2013; Palin et al., 2013). Additionally, FC-1
39 (Horstwood et al., 2003), Trebilcock (Tomascak et al., 1996) and Bananeira were also used as secondary
40 monazite RM, allowing $^{206}\text{Pb}/^{238}\text{U}$ ages to be within 2% of their accepted values. U-Pb proportions in
41 titanite were corrected using Bear Laken (Aleinikoff et al., 2007) and Y1710C5 (Spencer et al., 2013) as
42 RM. 91500 (Wieldenbeck et al., 1995) and GJI (Jackson et al., 2004) were used as RM for zircon, both
43 for isotopic composition and trace element calibrations. Radiogenic lead versus common lead
44 ($^{207}\text{Pb}/^{206}\text{Pb}$) measurements require up to 2% additional external error attributable either to variation count
45 statistics, or ablation signal stability (Spencer et al., 2013; Hacker et al., 2015b). These external errors
46 were incorporated into the data in the experiments.

47 The Iolite plug-in v. 2.5 (Paton et al., 2011) for the Wavemetrics Igor Pro software was used to
48 improve and reduce the analyses (Hacker et al., 2015). The isotopic ratios $^{238}\text{U}/^{206}\text{Pb}$ and $^{207}\text{Pb}/^{206}\text{Pb}$ for

1 each analysis were plotted on Tera-Wasserburg diagrams using Isoplot and Topsoil programs (Ludwig,
2 2012; Zeringue et al., 2014). All date uncertainties are reported at the 95% confidence interval, assuming
3 a Gaussian distribution of measurement errors. Zircon, titanite, and monazite REE analyses were
4 normalized against the McDonough and Sun (1995) chondrite values.

5 4. Results

6 4.1. Titanite (amphibolite, intermediate tectonic slice)

7 Fifty-one titanite analyses were projected onto a Tera-Wasserburg concordia plot (Fig. 3a). After
8 a preliminary evaluation, twelve analyses were rejected due to either high common Pb or high
9 discordance (>10%) and were considered no further (Table 1). The remaining analyses define a Pb/U
10 semi-total isochron between the common or initial Pb (^{207}Pb) and radiogenic Pb (^{206}Pb) (Ludwig, 1998).
11 The good fit of the isochron confirms the chemical homogeneity of the data (Stearns et al., 2016) and it
12 intercepts the concordia at 364.8 ± 4.5 Ma (2σ). Titanite chondrite-normalized REE analyses are detailed
13 in Table 1 and are shown in Fig. 3b. Titanite REE patterns are convex upwards, relatively flat, with slight
14 LREE depletions versus HREE with respect to chondrite. They generally lack a europium anomaly (Eu*),
15 but some analyses show a non-distinctive positive or negative anomaly. Recrystallized titanite, in the
16 presence of amphibole, show a similar REE pattern to them (Chambefort et al., 2013), with an umbrella
17 shape, suggesting a metamorphic origin (Mulrooney and Rivers, 2005; Lesnov, 2013).

18 4.2. Monazite (paragneiss, upper tectonic slice)

19 For monazite U/Th-Pb geochronology, we used the thorium zoning in monazite grains to select
20 the analytic spots. As shown in Figure 4 there are no significant age differences between spots or zones
21 with different Th chemical concentrations in a single grain. The obtained REE patterns are also very
22 similar, and the mismatch at the HREE is probably due to either uncertainties in measurement because of
23 the lower counts or interference effects of intermediate rare-earth oxides (Holder et al., 2015).

24 Data from seventy-six U/Th-Pb monazite analyses are shown in Table 2 and displayed using a
25 Tera-Wasserburg concordia plot (Fig. 5a). Four of these analyses, not related to chemical zoning, were
26 discarded due to common Pb loss and were considered no further. The remaining analyses form a single
27 population (mean square of weighted deviation; MSWD = 0.48) centered on a concordia age of $382.5 \pm$
28 1.0 Ma (2σ). Monazite geochemistry is shown in Figure 5b. REE patterns analyzed show an LREE
29 enrichment, HREE depletion and negative Y anomalies with respect to chondrite with little variation
30 within or between samples. The chemical profiles suggest simultaneous crystallization of monazite with
31 garnet (Rubatto, 2002; Rubatto et al., 2006; Mottram et al., 2014; Holder et al., 2015), which is stable at
32 paragneisses typical temperatures and pressures. Negative Eu anomalies indicate a preferential
33 incorporation of europium to feldspars, in particular to K-feldspar, during melt crystallization (Buick et
34 al., 2010; Rubatto et al., 2013). These characteristics are compatible with monazite recrystallization in a
35 single pulse (MSWD <1) in the presence of garnet, suggesting a metamorphic origin.

36 4.3. U-Pb zircon (paragneiss, upper tectonic slice)

37 Eighty-three analyses were performed on eighty zircon grains from the Sobrado paragneiss
38 (Table 3). In a preliminary assessment of the data two analyses were rejected due to analytical errors
39 (grain numbers 8, 36). Additionally, 23 analysis yielded a discordance higher than 10% and will not be
40 further considered. The remaining 58 zircon analyses are shown on a Wetherill concordia plot (Fig. 6a).
41 The $^{207}\text{Pb}/^{206}\text{Pb}$ ages older than 1000 Ma are presented in a probability density plot (Fig. 6b). Most of the
42 old ages are distributed between 1880 and 2200 Ma, with two peaks at 2030 and 2100 Ma. Three ages are
43 older, around 2600 Ma, and there are also two analysis around 1300 Ma. The $^{206}\text{Pb}/^{238}\text{U}$ ages younger
44 than 1000 Ma are plotted in a Tera-Wasserburg concordia plot (Fig. 7a) and a probability density plot
45 (Fig. 7b).

46 The data are continuously distributed between 589 and 380 Ma and attending to their CL texture,
47 ages from 589 to 510 Ma are obtained mainly from internal areas with oscillatory or sector zoning (e.g.,

33, 27 and 62, see Fig. 2); whereas, ages from 510 to 380 Ma correspond to discordant rims that have homogeneous CL signal, except for some grains (e.g., 10, 11 and 26, see Fig. 2) that are cores with oscillatory or sector zoning.

In order to get more insight into the meaning of the data, we have plotted these ages versus the Th/U ratios (Fig. 8) and we recognized two main groups. The first group is a cluster of zircon analyses with ages between 589 and 510 Ma and Th/U values higher than 0.3. The second group defines a trend with negative correlation from 500 to 380 Ma and Th/U values from 0.01 to 0.13. This correlation between the age and the composition of zircon suggests that the age dispersion is related to an actual geological process and is not caused by lead loss. Additionally, five analyses do not match these groups (analyses 10, 11, 26, 61 and 63) as they have ages lower than 510 Ma but show high Th/U ratios (>0.13). These outliers could be analytical errors, but they also correspond to the exceptions in the 510-380 Ma group, so they could be the result of a decoupling between the age and the composition (e.g., Flowers et al., 2012).

From the first group of data between 589 and 510 Ma, we can extract two ages, 546 ± 5 Ma out of six analyses, and 526 ± 3 Ma from 14 analyses (Fig. 9).

4.4. REE zircon (paragneiss, upper tectonic slice)

The chondrite-normalized REE patterns of the zircons with ages older than 600 Ma are shown in Figure 10a. In general, this group has REE patterns characteristic of igneous zircon (Hoskin and Schaltegger, 2003; Whitehouse and Platt, 2003; Hanchar and Westrenen, 2007; Grimes et al., 2015), with a pronounced fractionation from light to heavy REE and two anomalies in Ce (positive) and in Eu (negative). There are only three analyses that diverge from this template and show a flat HREE pattern that can be related to the presence of garnet and interpreted as metamorphic zircon.

For the younger analyses, the chondrite-normalized REE patterns have different features depending on the age group already defined (Fig. 10b). The oldest group (589-510 Ma) shows a tight HREE fractionation, variable Eu anomaly, and a pronounced Ce anomaly, all consistent with a magmatic origin. The youngest group (510-380 Ma) has a variable HREE slope, whereas the Eu anomaly is more regular, and the Ce anomaly is less marked. These features are compatible a metamorphic origin (Chen et al., 2009, 2010; Rubatto et al., 2009; Peters et al., 2013; Stipska et al., 2016).

When we plot Hf, Yb/Gd and Eu/Eu* against the ages for the young analyses (Fig. 11a, b, c), we can observe a great variation in composition of the 589-510 Ma group, but without a clear correlation. The group of outliers (excepting analysis 63 which has an anomalous composition) usually fits the composition of the first group, but at a younger age. Finally, in the 510-380 Ma group it is remarkable not only the good correlation between age and composition, but also the contrasting evolution depending of the age (grey arrows). Hafnium, Yb/Gd and Eu/Eu* increase from 510 to ~430 Ma while there is a striking decrease from ~420 to 380 Ma. These compositional variations suggest that the age smear observed between 510 and 380 Ma is not caused by lead loss, but it is related to the evolution of the hosting rocks. Finally, we have used the U/Ce-Th graph proposed by Bacon et al. (2012) to discriminate between metamorphic and igneous zircon. In this diagram, the first group of zircon and the outliers plot in the igneous zircon field, whereas the second group of zircon is projected in the metamorphic zircon field (Fig. 11d).

5. Discussion

5.1. Zircon inheritance

Based on CL images, ages and zircon composition, we can determine that the youngest zircon with magmatic origin is grain number 34 (Fig. 2), that yielded an age of 517 Ma. This age is comparable to other maximum depositional ages obtained from similar units in the NW Iberia allochthonous complexes, such as the intermediate-P Betanzos uppermost unit (530-510 Ma, Fuenlabrada et al., 2010), and the intermediate-P Cariño uppermost unit (~510 Ma, Albert et al., 2015). Older ages are interpreted

1 as inheritance mostly of magmatic provenance. The youngest magmatic episodes represented (546 and
2 526 Ma) in our sample are also recognized in other well-characterized high P-high T units of the
3 allochthonous complexes (Peucat et al., 1990; Santos Zalduegui et al., 2002; Castiñeiras et al., 2010), and
4 is related to a magmatic arc creation around the periphery of Gondwana (Abati et al., 1999, 2007).

5 U-Pb geochronology studies of detrital zircons and Sm-Nd whole rock analyses in intermediate-
6 P units of NW Iberia upper allochthons (Betanzos unit, Fuenlabrada et al., 2010; Cariño gneisses, Albert
7 et al., 2015) may give an indication of the provenance of inherited zircons older than 1000 Ma in the
8 Sobrado migmatitic paragneisses (Fig. 6b). We obtained two Mesoproterozoic analyses, between 1.2 and
9 1.4 Ga. Similar ages are also found in the Parautochthonous (Díez Fernández et al., 2012), in the basal
10 allochthonous units (Díez Fernández et al., 2010) and, to a lesser extent, in the intermediate-P units of
11 NW Iberia (Albert et al., 2015). These inherited zircons, although scarce (Fernández-Suárez et al., 2003),
12 likely have their origin in rocks derived from Saharan and Arabian-Nubian cratons, and presumably
13 transported during the Cadomian orogeny (e.g., Martínez Catalán et al., 2004). Paleoproterozoic
14 populations range from 1.8 to 2.2 Ga, clustered at 2.1 Ga, are also common in the Allochthonous
15 complexes (Fernández-Suárez et al., 2003) and their origin likely involves materials generated or
16 reworked during the Eburnian orogeny (e.g., Egal et al., 2002; Ennih and Liegeois, 2008) from the West
17 African craton (Peucat et al., 2005). Finally, the Archean population in the Sobrado paragneisses ranges
18 from 2.5 to 2.8 Ga, and it is likely related to intrusive events in the Western Reguibat Shield (Schofield et
19 al., 2012) and the northern part of the West African craton (Albert et al., 2015), with some reworking
20 processes of juvenile rocks formed at ca. 3.0 Ga (Potrel et al., 1998).

21 5.2. Evolution of metamorphism of the Sobrado migmatitic paragneiss based on zircon 22 composition

23 Extracting ages from a dataset where the data are evenly distributed from 502 to 380 Ma is a
24 challenging task. When such smear in the age sorting happens, if we can rule out analytical error, we have
25 three possibilities (e.g., Castiñeiras et al., 2010), namely, (i) the correct age is the youngest and the
26 dispersion is related to zircon inheritance, (ii) the real age is the oldest and the spread is caused by lead
27 loss, or, (iii) the age range is recording some kind of protracted geological event. Taking into account the
28 CL texture of the youngest spots, we can remove the first possibility as the majority of analyses were
29 performed in zircon rims. Furthermore, maximum depositional ages obtained from similar units from the
30 Allochthonous complex preclude their interpretation as inheritance. The second possibility is plausible,
31 considering the complex metamorphic evolution and the high grade attained by these rocks. However, a
32 young lead loss episode should have affected also the inherited zircon ages, and the presence of various
33 old age peaks (e.g., ~2000, 546 and 536 Ma) suggests that they did not experienced lead loss. Finally, the
34 strong correlation between age and zircon composition clearly points out to the validity of the third
35 option.

36 Even though the Th/U ratio shows a consistent evolution from 510 to 380 Ma, the rest of the
37 proxies considered (Hf, Yb/Gd and Eu/Eu*) point out to a two-stage evolution. This is compatible with
38 the presence of two metamorphic events in the HP-HT units, one at ~490-480 Ma and other at ~390-380
39 Ma (e.g., Fernández-Suárez et al., 2002, 2007). The increase recorded in Yb/Gd (Fig. 11b), related to the
40 slope of the HREE, from 502 to 430 Ma is congruent with a higher availability of HREE in the rock. As
41 garnet is the most important HREE reservoir in metamorphic rocks, we argue that this trend is recording
42 the progressive destabilization of garnet in a decompressive path from HP-HT conditions. The increase
43 observed in the Eu/Eu* ratio is consistent with a progressive retrogression of anortite, which is the main
44 europium reservoir in rocks (Barth and Wooden, 2010; Castiñeiras et al., 2011).

45 The sharp decrease observed in the Yb/Gd ratio from 420 to 380 Ma, is probably related to a
46 new event of garnet growth (Rubatto et al., 2006; Stipska et al., 2016), i.e., the second HP-HT event. The
47 evolution in the Eu/Eu* ratio suggests that this event took place under granulite facies conditions, as
48 plagioclase was present to pump out all the available europium.

5.3. Age of metamorphism in the Sobrado antiform

The youngest zircon data recorded (380 ± 4 Ma) is coherent with the monazite concordia age (382 ± 1 Ma) in the migmatitic paragneisses of the upper tectonic slice. This Middle Devonian age can be interpreted to represent the *minimum* age of the youngest metamorphic event in Sobrado unit, which reached high-P granulite facies (Fernández-Suárez et al., 2007; Ordóñez Casado et al., 2001). It is suggested that the recrystallized monazite captures the onset of the exhumation process in the migmatitic paragneisses (Holder et al., 2015). Titanite recrystallized, within the mylonitized amphibolites of the intermediate tectonic slice, in the Late Devonian (~ 365 Ma) and could be related to the onset of retrograde metamorphic conditions. This variation could be generated by the prolongation of the exhumation process, reaching amphibolite facies. The Late Devonian age lies close to the Ar/A_{K} (376 \pm 2.0 Ma), proposed for uppermost units of the Órdenes complex (Dallmeyer et al., 1997).

The U-Pb zircon age for the onset of the oldest metamorphic event was estimated using the TuffZirc method, developed by Ludwig and Mundil (2002), which calculates the median by choosing the largest set of concordant analyses that are statistically coherent. The best estimate obtained for this event is 489.58 (+ 12.15 - 6.76) Ma, obtained by pooling together only six of sixteen analyses (Fig. 12). The 510-380 Ma zircon aliquot shows a clear correlation between its cathodoluminescence texture and its geochemistry. The age recorded in the migmatitic paragneisses is thought to correspond to a metamorphic event, dated in the Early Ordovician (~ 490 Ma), and is in very good agreement with upper high-P/high-T dates of equivalent units carried out during previous studies (Kuijper, 1979; Peucat et al., 1990; Fernández-Suárez et al., 2002, 2007). This age also coincides with those obtained from intermediate pressure (intermediate-P) units, where large plutons were emplaced and there is a lack of later high-P/high-T metamorphism during the Devonian. The westernmost upper intermediate-P units of the Órdenes Complex underwent a granulite-facies metamorphism dated between ca. 500 and 485 Ma, contemporaneous with the intrusion of massive gabbros and granodiorites related to Cambrian magmatic arc activity (Abati et al., 1999, 2003, 2007, 1999; Andonaegui et al., 2002, 2012, 2016; Castiñeiras et al., 2002, 2010). The granulite-facies metamorphism is associated with heating produced by the intrusions, accompanied by a quick burial, almost coeval with igneous emplacement (Abati et al., 2003; Castiñeiras, 2005; Fernández-Suárez et al., 2007).

Clearly, the metamorphic event recorded in zircon is pre-Variscan and it is therefore independent of the high-P/high-T granulite-facies metamorphism that occurred during the Early-Middle Devonian that has been identified in the underlying upper units such as Sobrado with 660-770°C and 13-17 kbar (Arenas and Martínez Catalán, 2002), or 750-853°C and 11.5-15.4 kbar (Benítez-Pérez, 2017). Thus, not only was the pre-Variscan metamorphism followed by a decompression stage that was associated with partial melting (Fernández-Suárez et al., 2002), but also, later Devonian metamorphism and decompression during exhumation occurred, leading to partial melting in paragneisses and basic granulites (Fernández-Suárez et al., 2007). As the zircon composition clearly suggests, the notable slope observed in the TuffZirc plot from 489 to 380 Ma (Fig. 12) is the result of these exhumation, burial and new exhumation processes accompanied by partial melting.

6. Conclusions

This study provides new age constraints on the processes that have affected the Sobrado unit, part of the Órdenes Complex, and allows some correlation with events recognized in other parts of the allochthonous high-P/high-T complexes of NW Iberia. Titanite, monazite and zircon dating, together with REE analyses have been combined together in these rocks for the first time in order to carry out a geochronological investigation of the amphibolites and paragneisses.

According to the analyses, the youngest ages recorded by the metamorphic zircons are coherent with the concordia monazite age obtained from seventy-six analyses in the paragneisses. The Middle Devonian age (~ 380 Ma) represents the minimum age of the last Sobrado metamorphic event under high-P granulite-facies conditions and represents the first stages of the Variscan orogeny in this part of Iberia.

1 Dating of metamorphic titanite in the amphibolite yields a Late Devonian age (~365 Ma) and is
2 associated with very homogeneous REE patterns suggesting the prolongation of the exhumation process
3 in the Sobrado unit, reaching amphibolite-facies metamorphic conditions. In zircon, there is a strong
4 relationship between their textures, as seen in cathodoluminescence images (CL), REE patterns and
5 $^{206}\text{Pb}/^{238}\text{U}$ ages. Metamorphic zircon defines an Early Ordovician age (~490 Ma) although showing a
6 large dispersion. This date is linked to the first pre-Variscan granulite-facies metamorphism seen in in
7 Sobrado unit under intermediate-P conditions, and it is interpreted to be related to the intrusion of basic
8 and intermediate composition rocks, and coeval with burial in a magmatic arc context.

9 The maximum depositional age of the Sobrado unit is suggested to be late Cambrian based on the
10 age of the youngest inherited zircon (511 Ma). From the youngest set of inherited zircon, two ages can be
11 obtained (546 and 526 Ma) , pointing to the formation of a peri-Gondwana magmatic arc. The protoliths
12 of inherited zircon older than 1000 Ma from the Sobrado unit are found in other Iberian complexes and
13 are thought to be related to sources mainly in the West African craton.

14 *Data availability*

15 The data are not publicly accessible

16 *Supplement*

17 There is no supplement related to this article.

18 *Author contributions*

19 JMBP, PC, JGB and JRMC contributed equally to the field, experimental and elaboration of the
20 manuscript. AKC contributes to U-Pb-REE acquisition and data reduction and RH participated in the
21 writing of the text and the geological interpretation.

22 *Competing interests*

23 The authors declare that they have no conflict of interest.

24 **Acknowledgements**

25 This paper has been funded by the research projects CGL2011-22728 and CGL2016-78560-P of
26 the Spanish Ministry of Economy, Industry and Competitiveness, as part of the National Program of
27 Projects in Fundamental Research. JMBP appreciate financial support by the Spanish Ministry of
28 Economy, Industry and Competitiveness through the Formación de Profesional Investigador grant FPI
29 2013-2016 (BES-2012-059893). JGB appreciates financial support by the Spanish Ministry of Science
30 and Innovation through the IEDI-2016-00691 fellowship. We kindly appreciate excellent reviews from M.
31 Zucali and an anonymous referee which improved the manuscript.

32 **References**

- 33 Abati, J., Dunning, G.R., Arenas, R., Díaz García, F., González Cuadra, P., Martínez Catalán, J.R.,
34 Andonaegui, P., 1999. Early Ordovician orogenic event in Galicia (NW Spain): Evidence from U-Pb ages
35 in the uppermost unit of the Ordenes Complex. *Earth and Planetary Science Letters* 165, 213–228.
36 doi:10.1016/S0012-821X(98)00268-4
- 37 Abati, J., Arenas, R., Martínez Catalán, J.R., Díaz García, F., 2003. Anticlockwise P-T Path of Granulites
38 from the Monte Castelo Gabbro (Ordenes Complex, NW Spain). *Journal of Petrology* 44, 305–327.
39 doi:10.1093/petrology/44.2.305

- 1 Abati, J., Castiñeiras, P., Arenas, R., Fernández-Suárez, J., Barreiro, J.G., Wooden, J.L., 2007. Using
2 SHRIMP zircon dating to unravel tectonothermal events in arc environments. The early Palaeozoic arc of
3 NW Iberia revisited. *Terra Nova* 19, 432–439. doi:10.1111/j.1365-3121.2007.00768.x
- 4 Abati, J., Gerdes, A., Suárez, J.F., Arenas, R., Whitehouse, M.J., Fernández, R.D., 2010. Magmatism and
5 early-Variscan continental subduction in the northern Gondwana margin recorded in zircons from the
6 basal units of Galicia, NW Spain. *Bulletin of the Geological Society of America* 122, 219–235.
7 doi:10.1130/B26572.1
- 8 Aerden, D.G.A.M., 2004. Correlating deformation in Variscan NW-Iberia using porphyroblasts;
9 implications for the Ibero-Armorican Arc. *Journal of Structural Geology* 26, 177–196.
10 doi:10.1016/S0191-8141(03)00070-1
- 11 Albert, R., Arenas, R., Gerdes, A., Sánchez-Martínez, S., Fernández-Suárez, J., Fuenlabrada, J.M., 2015.
12 Provenance of the Variscan Upper Allochthon (Cabo Ortegal Complex, NW Iberian Massif). *Gondwana*
13 *Research* 28, 1434–1448. doi:10.1016/j.gr.2014.10.016
- 14 Aleinikoff, J.N., Schenck, W.S., Plank, M.O., Srogi, L.A., Fanning, C.M., Kamo, S.L., Bosbyshell, H.,
15 2006. Deciphering igneous and metamorphic events in high-grade rocks of the Wilmington complex,
16 Delaware: Morphology, cathodoluminescence and backscattered electron zoning, and SHRIMP U-Pb
17 geochronology of zircon and monazite. *Bulletin of the Geological Society of America* 118, 39–64.
18 doi:10.1130/B25659.1
- 19 Aleinikoff, J.N., Wintsch, R.P., Tollo, R.P., Unruh, D.M., Fanning, C.M., Schmitz, M.D., 2007. Ages and
20 origins of rocks of the Killingworth dome, south-central Connecticut: Implications for the tectonic
21 evolution of southern New England. *American Journal of Science* 307, 63–118. doi:10.2475/01.2007.04
- 22 Álvarez-Valero, A.M., Gómez-Barreiro, J., Alampi, A., Castiñeiras, P., Martínez Catalán, J.R., 2014.
23 Local isobaric heating above an extensional detachment in the middle crust of a Variscan allochthonous
24 terrane (Ordenes complex, NW Spain). *Lithosphere* 6, 409–418. doi:10.1130/L369.1
- 25 Andonaegui, P., Castiñeiras, P., González Cuadra, P., Arenas, R., Sánchez Martínez, S., Abati, J., Díaz
26 García, F., Martínez Catalán, J.R., 2012. The Corredoiras orthogneiss (NW Iberian Massif):
27 Geochemistry and geochronology of the Paleozoic magmatic suite developed in a peri-Gondwanan arc.
28 *Lithos* 128–131, 84–99. doi:10.1016/j.lithos.2011.11.005
- 29 Andonaegui, P., González Del Tánago, J., Arenas, R., Abati, J., Martínez Catalán, J.R., Peinado, M., Díaz
30 García, F., 2002. Tectonic setting of the Monte Castelo gabbro (Ordenes Complex, northwestern Iberian
31 Massif): Evidence for an arc-related terrane in the hanging wall to the Variscan suture. *Special Paper of*
32 *the Geological Society of America* 364, 37–56. doi:10.1130/0-8137-2364-7.37
- 33 Andonaegui, P., Sánchez-Martínez, S., Castiñeiras, P., Abati, J., Arenas, R., 2016. Reconstructing
34 subduction polarity through the geochemistry of mafic rocks in a Cambrian magmatic arc along the
35 Gondwana margin (Órdenes Complex, NW Iberian Massif). *International Journal of Earth Sciences* 105,
36 713–725. doi:10.1007/s00531-015-1195-x
- 37 Arenas, R., Martínez Catalán, J.R., 2002. Prograde development of corona textures in metagabbros of the
38 Sobrado unit (Ordenes Complex, northwestern Iberian Massif). *Geological Society of America Special*
39 *Pa*, 73–88. doi:10.1130/0-8137-2364-7.73
- 40 Bacon, C.R., Vazquez, J.A., Wooden, J.L., 2012. Peninsular terrane basement ages recorded by Paleozoic
41 and Paleoproterozoic zircon in gabbro xenoliths and andesite from Redoubt volcano, Alaska. *Bulletin of*
42 *the Geological Society of America* 124, 24–34. doi:10.1130/B30439.1
- 43 Ballèvre, M., Martínez Catalán J.R., López-Carmona, A., Pitra, P., Abati, J., Díez Fernández, R.,
44 Ducassou, C., Arenas, R., Bosse, V., Castiñeiras, P., Fernández-Suárez, J., Gómez Barreiro, J., Paquette,
45 J-L., Peucat, J-J, Poujol, M., Ruffet, G. and Sánchez Martínez, S., 2014. Correlation of the nappe stack in

- 1 the Ibero-Armorican arc across the Bay of Biscay: a joint French–Spanish project. Geological Society,
2 London, Special Publications, 405, .doi: 10.1144/SP405.13
- 3 Barth, A.P., Wooden, J.L., 2010. Coupled elemental and isotopic analyses of polygenetic zircons from
4 granitic rocks by ion microprobe, with implications for melt evolution and the sources of granitic
5 magmas. *Chemical Geology* 277, 149–159. doi:10.1016/j.chemgeo.2010.07.017
- 6 Belousova, E.A., Griffin, W.L., O'Reilly, S.Y., Fisher, N.I., 2002. Igneous zircon: trace element
7 composition as an indicator of source rock type. *Contributions to Mineralogy and Petrology* 143, 602–
8 622. doi:10.1007/s00410-002-0364-7
- 9 Benítez-Pérez, J.M., 2017. Quantitative study of texture in tectonites by diffraction. Contribution to
10 seismic anisotropy and orogenic rheology. University of Salamanca (PhD. Thesis). Spain.
- 11 Buick, I.S., Clark, C., Rubatto, D., Hermann, J., Pandit, M., Hand, M., 2010. Constraints on the
12 Proterozoic evolution of the Aravalli-Delhi Orogenic belt (NW India) from monazite geochronology and
13 mineral trace element geochemistry. *Lithos* 120, 511–528. doi:10.1016/j.lithos.2010.09.011
- 14 Castiñeiras, P., Andonaegui, P., Arenas, R., Martínez Catalán, J., 2002. Descripción y resultados
15 preliminares del plutón compuesto de San Xiao, Complejo de Cabo Ortegal (noroeste del Macizo
16 Ibérico). *Geogaceta* 32, 111–114.
- 17 Castiñeiras, P., 2005. Origen y evolución tectonotermal de las unidades de O Pino y Cariño (Complejos
18 Alóctonos de Galicia). *Laboratorio Xeolóxico de Laxe, Serie Nova Terra*, 28, A Coruña.
- 19 Castiñeiras, P., García, F.D., Gómez-Barreiro, J., 2010. REE-assisted U-Pb zircon age (SHRIMP) of an
20 anatectic granodiorite: Constraints on the evolution of the A Silva granodiorite, Iberian allochthonous
21 complexes. *Lithos* 116, 153–166. doi:10.1016/j.lithos.2010.01.013
- 22 Castiñeiras, P., Navidad, M., Casas, J.M., Liesa, M., Carreras, J., 2011. Petrogenesis of Ordovician
23 Magmatism in the Pyrenees (Albera and Canigó Massifs) Determined on the Basis of Zircon Minor and
24 Trace Element Composition. *The Journal of Geology* 119, 521–534. doi:10.1086/660889
- 25 Chen, R.X., Zheng, Y.F., Xie, L., 2010. Metamorphic growth and recrystallization of zircon: Distinction
26 by simultaneous in-situ analyses of trace elements, U-Th-Pb and Lu-Hf isotopes in zircons from eclogite-
27 facies rocks in the Sulu orogen. *Lithos* 114, 132–154. doi:10.1016/j.lithos.2009.08.006
- 28 Cheng, H., King, R.L., Nakamura, E., Vervoort, J.D., Zheng, Y.F., Ota, T., Wu, Y.B., Kobayashi, K.,
29 Zhou, Z.Y., 2009. Transitional time of oceanic to continental subduction in the Dabie orogen: Constraints
30 from U-Pb, Lu-Hf, Sm-Nd and Ar-Ar multichronometric dating. *Lithos* 110, 327–342.
31 doi:10.1016/j.lithos.2009.01.013
- 32 Cherniak, D.J., 2006. Zr diffusion in titanite. *Contributions to Mineralogy and Petrology* 152, 639–647.
33 doi:10.1007/s00410-006-0133-0
- 34 Corfu, F., Hanchar, J.M., Hoskin, P.W.O., Kinny, P.D., 2003. Atlas of Zircon Textures, in: Hanchar,
35 J.M., Hoskin, P.W.O. (Eds.), *Zircon. Reviews in Mineralogy and Geochemistry*. Mineralogical Society of
36 America, pp. 468–500.
- 37 Corrie, S.L., Kohn, M.J., 2008. Trace-element distributions in silicates during prograde metamorphic
38 reactions : implications for monazite formation 451–464. doi:10.1111/j.1525-1314.2008.00769.x
- 39 Dallmeyer, R.D., Martínez Catalán, J.R., Arenas, R., Gil Ibarguchi, J.I., Gutiérrez-Alonso, G., Farias, P.,
40 Bastida, F., Aller, J., 1997. Diachronous Variscan tectonothermal activity in the NW Iberian Massif:
41 Evidence from $^{40}\text{Ar}/^{39}\text{Ar}$ dating of regional fabrics. *Tectonophysics* 277, 307–337. doi:10.1016/S0040-
42 1951(97)00035-8

- 1 Dallmeyer, R.D., Ribeiro, A., Marques, F., 1991. Polyphase Variscan emplacement of exotic terranes
2 (Morais and Bragança Massifs) onto Iberian successions: Evidence from ⁴⁰Ar/³⁹Ar mineral ages. *Lithos*
3 27, 133–144. doi:10.1016/0024-4937(91)90025-G
- 4 DeWolf, C.P., Belshaw, N., O’Nions, R.K., 1993. A metamorphic history from micron-scale
5 ²⁰⁷Pb/²⁰⁶Pb chronometry of Archean monazite. *Earth and Planetary Science Letters* 120, 207–220.
- 6 Dias da Silva, I., Valverde-Vaquero, P., González-Clavijo, E., Díez-Montes, A. y Martínez Catalán, J. R.
7 2014. Structural and stratigraphical significance of U–Pb ages from the Mora and Saldanha volcanic
8 complexes (NE Portugal, Iberian Variscides). In: Schulmann, K., Martínez Catalán, J. R., Lardeaux, J.
9 M., Janousek, V. & Oggiano, G. (eds) *The Variscan Orogeny: Extent, Timescale, the Formation of the*
10 *European Crust*. Geological Society, London, Special Publications, 405. First published online February
11 25, 2014, <http://dx.doi.org/10.1144/SP405.3>
- 12 Díaz García, F., Martínez Catalán, J.R., Arenas, R., González Cuadra, P., 1999. Structural and kinematic
13 analysis of the Corredoiras detachment: evidence for early Variscan synconvergent extension in the
14 Ordenes Complex, NW Spain. *International Journal of Earth Sciences* 88, 337–351.
- 15 Dickinson, W.R., Gehrels, G.E., 2009. Use of U–Pb ages of detrital zircons to infer maximum
16 depositional ages of strata: A test against a Colorado Plateau Mesozoic database. *Earth and Planetary*
17 *Science Letters* 288, 115–125. doi:10.1016/j.epsl.2009.09.013
- 18 Díez Fernández, R., Catalán, J.R.M., Gerdes, A., Abati, J., Arenas, R., Fernández-Suárez, J., 2010. U–Pb
19 ages of detrital zircons from the Basal allochthonous units of NW Iberia: Provenance and paleoposition
20 on the northern margin of Gondwana during the Neoproterozoic and Paleozoic. *Gondwana Research* 18,
21 385–399. doi:10.1016/j.gr.2009.12.006
- 22 Díez Fernández, R., Martínez Catalán, J.R., Arenas, R., Abati, J., Gerdes, A., Fernández-Suárez, J., 2012.
23 U–Pb detrital zircon analysis of the lower allochthon of NW Iberia: age constraints, provenance and links
24 with the Variscan mobile belt and Gondwanan cratons. *Journal of the Geological Society* 169, 655–665.
25 doi:10.1144/jgs2011-146
- 26 Egal, E., Thiéblemont, D., Lahondère, D., Guerrot, C., Costea, C.A., Iliescu, D., Delor, C., Goujou, J.C.,
27 Lafon, J.M., Tegye, M., Diaby, S., Kolié, P., 2002. Late Eburnean granitization and tectonics along the
28 western and northwestern margin of the Archean Koma-Man domain (Guinea, West African Craton).
29 *Precambrian Research* 117, 57–84. doi:10.1016/S0301-9268(02)00060-8
- 30 Ennih, N., Liegeois, J.-P., 2008. The boundaries of the West African craton, with special reference to the
31 basement of the Moroccan metacratonic Anti-Atlas belt. *The Boundaries of the West African Craton* 1–
32 17. doi:10.1144/SP297.1
- 33 Farias, P., Gallastegui, G. et al. 1987. Aportaciones al conocimiento de la litoestratigrafía y estructura de
34 Galicia Central. *Memoórias da Faculdade de Ciências, Universidade do Porto*, 1, 411–431.
- 35 Fernández-Suárez, J., Arenas, R., Abati, J., Martínez Catalán, J.R., Whitehouse, M., Jeffries, T., 2007.
36 U–Pb chronometry of polymetamorphic high-pressure granulites: An example from the allochthonous
37 terranes of the NW Iberian Variscan belt. *Geological Society of America Memoir*, 469–488.
38 doi:10.1130/2007.1200(24).
- 39 Fernández-Suárez, J., Corfu, F., Arenas, R., Marcos, A., Martínez Catalán, J.R., Díaz García, F., Abati, J.,
40 Fernández, F.J., 2002. U–Pb evidence for a polyorogenic evolution of the HP-HT units of the NW Iberian
41 Massif. *Contributions to Mineralogy and Petrology* 143, 236–253. doi:10.1007/s00410-001-0337-2
- 42 Fernández-Suárez, J., García, F.D., Jeffries, T.E., Arenas, R., 2003. Constraints on the provenance of the
43 uppermost allochthonous terrane of the NW Iberian Massif: inferences from detrital zircon U–Pb ages.
44 *Terra Nova* 15, 138–144.

- 1 Franz, G., Spear, F.S., 1985. Aluminous Titanite (sphene) from the eclogite zone, south-central Tauern
2 window, Austria. *Chemical Geology* 50, 33–46.
- 3 Frost, B.R., Chamberlain, K.R., Schumacher, J.C., 2000. Sphene (titanite): phase relations and role as a
4 geochronometer. *Chemical Geology* 172, 131–148.
- 5 Fuenlabrada, J., Arenas, R., Sánchez-Martínez, S., Díaz García, F., Castiñeiras, P., 2010. A peri-
6 Gondwanan arc in NW Iberia I: Isotopic and geochemical constraints on the origin of the arc-A
7 sedimentary approach. *Gondwana Research* 17, 338–351. doi:10.1016/j.gr.2009.09.007
- 8 Gagnevin, D., Daly, J.S., 2010. Zircon texture and chemical composition as a guide to magmatic
9 processes and mixing in a granitic environment and coeval volcanic system. doi:10.1007/s00410-009-
10 0443-0
- 11 Gómez-Barreiro, J., Martínez Catalán, J.R., Arenas, R., Castiñeiras, P., Abati, J., Díaz García, F.,
12 Wijbrans, J.R., 2007. Tectonic evolution of the upper allochthon of the Órdenes complex (northwestern
13 Iberian Massif): Structural constraints to a polyorogenic peri-Gondwanan terrane. *Geological Society of
14 America* 423, 315–332. doi:10.1130/2007.2423(15).
- 15 Goncalves, P., Williams, M.L., Jercinovic, M.J., 2005. Electron-microprobe age mapping of monazite.
16 *American Mineralogist* 90, 578–585. doi:10.2138/am.2005.1399
- 17 Grimes, C.B., Wooden, J.L., Cheadle, M.J., John, B.E., 2015. “Fingerprinting” tectono-magmatic
18 provenance using trace elements in igneous zircon. *Contributions to Mineralogy and Petrology* 170, 1–26.
19 doi:10.1007/s00410-015-1199-3
- 20 Gutiérrez-Alonso, G., Fernández-Suárez, J., Jeffries, T.E., Jenner, G.A., Tubrett, M.N., Cox, R., Jackson,
21 S.E., 2003. Terrane accretion and dispersal in the northern Gondwana margin. An Early Paleozoic
22 analogue of a long-lived active margin. *Tectonophysics* 365, 221–232. doi:10.1016/S0040-
23 1951(03)00023-4
- 24 Hacker, B.R., Kylander-clark, A.R.C., Holder, R., Andersen, T.B., Peterman, E.M., Walsh, E.O.,
25 Munnikhuis, J.K., 2015. Monazite response to ultrahigh-pressure subduction from U – Pb dating by laser
26 ablation split stream. *Chemical Geology* 409, 28–41. doi:10.1016/j.chemgeo.2015.05.008
- 27 Hanchar, J.M., Westrenen, W. Van, 2007. Rare earth element behavior in zircon–melt systems. *Elements*
28 3, 37–42.
- 29 Harlov, D., Tropper, P., Seifert, W., Nijland, T., Förster, H.-J., 2006. Formation of Al-rich titanite
30 ($\text{CaTiSiO}_4 \text{O} - \text{CaAlSiO}_4 \text{OH}$) reaction rims on ilmenite in metamorphic rocks as a function of $f \text{H}_2\text{O}$
31 and $f \text{O}_2$. *Lithos* 88, 72–84. doi:10.1016/j.lithos.2005.08.005
- 32 Hawkins, D.P., Bowring, S.A., 1997. U-Pb systematics of monazite and xenotime : case studies from the
33 Paleoproterozoic of the Grand Canyon, Arizona 87–103.
- 34 Hermann, J., Rubatto, D., 2003. Relating zircon and monazite domains to garnet growth zones : Age and
35 duration of granulite facies metamorphism in the Val Malenco lower crust. *Journal of Metamorphic* 21,
36 Issue 9. doi:10.1046/j.1525-1314.2003.00484.x
- 37 Hokada, T., Harley, S.L., 2004. Zircon growth in UHT leucosome: constraints from zircon-garnet rare
38 earth elements (REE) relations in Napier Complex, East Antarctica. *Journal of Mineralogical and
39 Petrological Sciences* 99, 180–190. doi:10.2465/jmps.99.180
- 40 Holder, R.M., Hacker, B.R., Kylander-clark, A.R.C., Cottle, J.M., 2015. Monazite trace-element and
41 isotopic signatures of (ultra) high-pressure metamorphism : Examples from the Western Gneiss Region,
42 Norway. *Chemical Geology* 409, 99–111. doi:10.1016/j.chemgeo.2015.04.021

- 1 Horstwood, M.S.A., Foster, G.L., Parrish, R.R., Noble, S.R., Nowell, G.M., 2003. Common-Pb corrected
2 in situ U–Pb accessory mineral geochronology by LA-MC-ICP-MS. *The Royal Society of Chemistry* 18,
3 837–846. doi:10.1039/b304365g
- 4 Hoskin, P.W.O., 2005. Trace-element composition of hydrothermal zircon and the alteration of Hadean
5 zircon from the Jack Hills, Australia. *Geochimica et Cosmochimica Acta* 69, 637–648.
6 doi:10.1016/j.gca.2004.07.006
- 7 Hoskin, P.W.O., Ireland, T.R., 2000. Rare earth element chemistry of zircon and its use as a provenance
8 indicator. *Geology* 28, 627–630. doi:10.1130/0091-7613(2000)28<627:REECOZ>2.0.CO
- 9 Hoskin, P.W.O., Schaltegger, U., 2003. The Composition of Zircon and Igneous and Metamorphic
10 Petrogenesis, in: Hanchar, J.M., Hoskin, P.W.O. (Eds.), *Zircon. Reviews in Mineralogy and*
11 *Geochemistry*. Mineralogical Society of America, pp. 27–62.
- 12 Jackson, S.E., Pearson, N.J., Griffin, W.L., Belousova, E.A., 2004. The application of laser ablation-
13 inductively coupled plasma-mass spectrometry to in situ U-Pb zircon geochronology. *Chemical Geology*
14 211, 47–69. doi:10.1016/j.chemgeo.2004.06.017
- 15 Kohn, M.J., Malloy, M.A., 2004. Formation of monazite via prograde metamorphic reactions among
16 common silicates : Implications for age determinations. *Geochimica et cosmochimica Acta* 68, 101–113.
17 doi:10.1016/S0016-7037(03)00258-8
- 18 Košler, J., Tubrett, M.N., Sylvester, P.J., 2001. Application of laser ablation ICP-MS to U-Th-Pb dating
19 of monazite. *Geostandards Newsletter-the Journal of Geostandards and Geoanalysis* 25, 375–386.
20 doi:10.1111/j.1751-908X.2001.tb00612.x
- 21 Kretz, R., 1983. Symbols for rock-forming minerals. *American Mineralogist* 68, 277–279.
22 doi:10.1016/0016-7037(83)90220-X
- 23 Kuijper, R.P., 1979. U-Pb systematic and petrogenetic evolution of infracrustal rocks in the Paleozoic
24 basement of Western Galicia, NW Iberia. WO Laboratory of Isotope Geology, Amsterdam.
- 25 Kylander-Clark, A.R.C., Hacker, B.R., Cottle, J.M., 2013. Laser-ablation split-stream ICP
26 petrochronology. *Chemical Geology* 345, 99–112. doi:10.1016/j.chemgeo.2013.02.019
- 27 Lesnov, F.P., 2013. Consistent patterns of rare earth element distribution in accessory minerals from
28 rocks of mafic-ultramafic complexes. *Central European Journal of Geosciences* 5, 112–173.
29 doi:10.2478/s13533-012-0121-z
- 30 Linnemann, U., Gerdes, A., Hofmann, M., Marko, L., 2014. The Cadomian Orogen: Neoproterozoic to
31 Early Cambrian crustal growth and orogenic zoning along the periphery of the West African Craton-
32 Constraints from U-Pb zircon ages and Hf isotopes (Schwarzburg Antiform, Germany). *Precambrian*
33 *Research* 244, 236–278. doi:10.1016/j.precamres.2013.08.007
- 34 Ludwig, K.R., 1998. On the Treatment of Concordant Uranium-Lead Ages. *Geochimica et*
35 *Cosmochimica Acta* 62, 665–676. doi:10.1016/S0016-7037(98)00059-3
- 36 Ludwig, K.R., Mundil, R., 2002. Extracting reliable U–Pb ages and errors from complex populations of
37 zircons from Phanerozoic tuffs. *Geochimica et Cosmochimica Acta* 66, 463.
- 38 Ludwig, K.R., 2012. User’s Manual for ISOPLOT version 3.75. A Geochronological Toolkit for
39 Microsoft Excel. Berkeley Geochronology Center.
- 40 Martínez Catalán, J.R., Arenas, R., Díaz García, F., Abati, J., 1999. Allochthonous Units in the Variscan
41 Belt of NW Iberia: Terranes and Accretionary History, in: Sinha, A.K. (Ed.), *Basement Tectonics 13:*
42 *Proceedings of the Thirteenth International Conference on Basement Tectonics Held in Blacksburg,*
43 *Virginia, U.S.A., June 1997.* Springer Netherlands, Dordrecht, pp. 65–84. doi:10.1007/978-94-011-4800-
44 9_5

- 1 Martínez Catalán, J.R., Fernández-Suárez, J., Jenner, G.A., Belousova, E., Díez Montes, A., 2004,
2 Provenance constraints from detrital zircon U–Pb ages in the NW Iberian Massif: implications for
3 Paleozoic plate configuration and Variscan evolution. *J. Geol. Soc. London*, 161, 461–473.
4 doi:10.1144/0016-764903-054
- 5 Martínez Catalán, J.R., Arenas, R., Abati, J., Sánchez Martínez, S., Díaz García, F., Fernández Suárez, J.,
6 González Cuadra, P., Castiñeiras, P., Gómez Barreiro, J., Díez Montes, A., González Clavijo, E., Rubio
7 Pascual, F.J., Andonaegui, P., Jeffries, T.E., Alcock, J.E., Díez Fernández, R., López Carmona, A., 2009.
8 A rootless suture and the loss of the roots of a mountain chain: The Variscan belt of NW Iberia. *Comptes*
9 *Rendus Geoscience* 341, 114–126. doi:10.1016/j.crte.2008.11.004
- 10 Martínez Catalán, J.R., 2011. Are the oroclines of the Variscan belt related to late Variscan strike-slip
11 tectonics? *Terra Nova* 23, 241–247. doi:10.1111/j.1365-3121.2011.01005.x
- 12 Martínez Catalán, J.R., 2012. The Central Iberian arc, an orocline centered in the Iberian Massif and some
13 implications for the Variscan belt. *International Journal of Earth Sciences* 101, 1299–1314.
14 doi:10.1007/s00531-011-0715-6
- 15 McDonough, W.F., Sun, S.S., 1995. The composition of the Earth. *Chemical Geology* 120, 223–253.
16 doi:10.1016/0009-2541(94)00140-4
- 17 Möller, A., O’Brien, P.J., Kennedy, A., Kröner, A., 2002. Polyphase zircon in ultrahigh-temperature
18 granulites (Rogaland, SW Norway): Constraints for Pb diffusion in zircon. *Journal of Metamorphic*
19 *Geology* 20, 727–740. doi:10.1046/j.1525-1314.2002.00400.x
- 20 Mottram, C.M., Warren, C.J., Regis, D., Roberts, N.M.W., Harris, N.B.W., Argles, T.W., Parrish, R.R.,
21 2014. Developing an inverted barrovian sequence; insights from monazite petrochronology. *Earth and*
22 *Planetary Science Letters* 403, 418–431. doi:10.1016/j.epsl.2014.07.006
- 23 Mulrooney, D., Rivers, T., 2005. Redistribution of the rare-earth elements among coexisting minerals in
24 metamafic rocks across the epidote-out isograd: An example from the St. Anthony Complex, northern
25 Newfoundland, Canada. *Canadian Mineralogist* 43, 263–294. doi:10.2113/gscanmin.43.1.263
- 26 Nasdala, L., Zhang, M., Kempe, U., Panczer, G., Gaft, M., Andrut, M., Plötze, M., 2003. Spectroscopic
27 methods applied to zircon, in: Hanchar, J.M., Hoskin, P.W.O. (Eds.), *Zircon. Reviews in Mineralogy and*
28 *Geochemistry*. Mineralogical Society of America, pp. 427–467.
- 29 Ordóñez Casado, B., 1998. Geochronological studies of the pre-Mesozoic basement of the Iberian
30 Massif: the Ossa Morena zone and the Allochthonous Complexes within the Central Iberian zone.
31 doi:10.3929/ethz-a-002017279
- 32 Ordóñez Casado, B., Gebauer, D., Schäfer, H.J., Ibarguchi, J.I.G., Peucat, J.J., 2001. A single Devonian
33 subduction event for the HP/HT metamorphism of the Cabo Ortegal complex within the Iberian Massif.
34 *Tectonophysics* 332, 359–385. doi:10.1016/S0040-1951(00)00210-9
- 35 Palin, R.M., Searle, M.P., Waters, D.J., Parrish, R.R., Roberts, N.M.W., Horstwood, M.S.A., Yeh, M.W.,
36 Chung, S.L., Anh, T.T., 2013. A geochronological and petrological study of anatexitic paragneiss and
37 associated granite dykes from the Day Nui Con Voi metamorphic core complex, North Vietnam:
38 Constraints on the timing of metamorphism within the Red River shear zone. *Journal of Metamorphic*
39 *Geology* 31, 359–387. doi:10.1111/jmg.12025
- 40 Paton, C., Hellstrom, J., Paul, B., Woodhead, J., Hergt, J., 2011. Iolite: Freeware for the visualisation and
41 processing of mass spectrometric data. *Journal of Analytical Atomic Spectrometry* 26, 2508.
42 doi:10.1039/c1ja10172b
- 43 Peters, T.J., Ayers, J.C., Gao, S., Liu, X.M., 2013. The origin and response of zircon in eclogite to
44 metamorphism during the multi-stage evolution of the Huwan Shear Zone, China: Insights from Lu-Hf

- 1 and U-Pb isotopic and trace element geochemistry. *Gondwana Research* 23, 726–747.
2 doi:10.1016/j.gr.2012.05.008
- 3 Peucat, J.J., Bernard Griffiths, J., Ibaguchi, J.I.G., Dallmeyer, R.D., Menot, R.P., Cornichet, J., Ponce de
4 León, M.I., 1990. Geochemical and Geochronological Cross-Section of the Deep Variscan Crust - the
5 Cabo-Ortega High-Pressure Nappe (Northwestern Spain). *Tectonophysics* 177, 263–292.
- 6 Peucat, J.J., Capdevila, R., Drareni, A., Mahdjoub, Y., Kahoui, M., 2005. The Eglab massif in the West
7 African Craton (Algeria), an original segment of the Eburnean orogenic belt: Petrology, geochemistry and
8 geochronology. *Precambrian Research* 136, 309–352. doi:10.1016/j.precamres.2004.12.002
- 9 Potrel, A., Peucat, J.J., Fanning, C.M., 1998. Archean crustal evolution of the West African Craton:
10 example of the Amsaga Area (Reguibat Rise). U-Pb and Sm-Nd evidence for crustal growth and
11 recycling. *Precambrian Research* 90, 107–117. doi:10.1016/S0301-9268(98)00044-8
- 12 Ribeiro, A., Pereira, E. & Dias, R. 1990. Central-Iberian Zone. Allochthonous Sequences. Structure in the
13 Northwest of the Iberian Peninsula. In: Dallmeyer, R. D. y Martínez García, E. (eds) *Pre-Mesozoic*
14 *Geology of Iberia*. Springer, Berlin, 220–236.
- 15 Rubatto, D., Hermann, J., 2001. Exhumation as fast as subduction? *Geology* 29, 3–6.
- 16 Rubatto, D., 2002. Zircon trace element geochemistry : distribution coefficients and the link between U-
17 Pb ages and metamorphism Zircon trace element geochemistry : partitioning with garnet and the link
18 between U – Pb ages and metamorphism. *Chemical Geology* 184, 123–138.
- 19 Rubatto, D., Hermann, R.G., Buick, I.S., 2006. Temperature and Bulk Composition Control on the
20 Growth of Monazite and Zircon During Low-pressure Anatexis (Mount Stafford , Central Australia).
21 *Journal of Petrology* 47, 1973–1996. doi:10.1093/petrology/egl033
- 22 Rubatto, D., Hermann, J., Berger, A., Engi, M., 2009. Protracted fluid-induced melting during Barrovian
23 metamorphism in the Central Alps. *Contributions to Mineralogy and Petrology* 158, 703–722.
24 doi:10.1007/s00410-009-0406-5
- 25 Rubatto, D., Chakraborty, S., Dasgupta, S., 2013. Timescales of crustal melting in the Higher Himalayan
26 Crystallines (Sikkim, Eastern Himalaya) inferred from trace element-constrained monazite and zircon
27 chronology. *Contributions to Mineralogy and Petrology* 165, 349–372. doi:10.1007/s00410-012-0812-y
- 28 Santos Zalduegui, J.F., Schärer, U., Gil Ibaguchi, J.I., 1995. Isotope constraints on the age and origin of
29 magmatism and metamorphism in the Malpica-Tuy allochthon, Galicia, NW Spain. *Chemical Geology*
30 121, 91–103. doi:10.1016/0009-2541(94)00123-P
- 31 Santos Zalduegui, J.F., Schärer, U., Gil Ibaguchi, J.I., Girardeau, J., 1996. Origin and evolution of the
32 Paleozoic Cabo Ortega ultramafic-mafic complex (NW Spain): U-Pb, Rb-Sr and Pb-Pb isotope data.
33 *Chemical Geology* 129, 281–304. doi:10.1016/0009-2541(95)00144-1
- 34 Santos Zalduegui, J.F., Scharer, U., Gil Ibaguchi, J.I., Girardeau, J., 2002. Genesis of Pyroxenite-rich
35 Peridotite at Cabo Ortega (NW Spain): Geochemical and Pb-Sr-Nd Isotope Data. *J. Petrol.* 43, 17–43.
36 doi:10.1093/petrology/43.1.17
- 37 Schaltegger, U., Fanning, C.M., Günter, D., Maurin, J.C., Schulmann, K., Gebauer, D., 1999. Growth,
38 annealing and recrystallization of zircon and preservation of monazite in high-grade metamorphism:
39 conventional and in-situ U-Pb isotope, cathodoluminescence and microchemical evidence. *Contributions*
40 *to Mineralogy and Petrology* 134, 186–201.
- 41 Schofield, D.I., Horstwood, M.S.A., Pitfield, P.E.J., Gillespie, M., Darbyshire, F., O'Connor, E.A.,
42 Abdouloye, T.B., 2012. U-Pb dating and Sm-Nd isotopic analysis of granitic rocks from the Tiris
43 Complex: New constraints on key events in the evolution of the Reguibat Shield, Mauritania. *Precambrian*
44 *Research* 204–205, 1–11. doi:10.1016/j.precamres.2011.12.008

- 1 Spear, F.S., 1981. An experimental study of hornblende stability and compositional variability in
2 amphibolite. *American Journal of Science*. doi:10.2475/ajs.281.6.697
- 3 Spear, F.S., Pyle, J.M., 2002. Apatite , Monazite , and Xenotime in Metamorphic Rocks, in: Kohn, M.J.,
4 Rakovan, J., Hughes, J.M. (Eds.), *Phosphates: Geochemical, Geobiological, and Materials Importance*.
5 *Reviews in Mineralogy and Geochemistry*. doi:10.2138/rmg.2002.48.7
- 6 Spencer, K.J., Hacker, B.R., Kylander-clark, A.R.C., Andersen, T.B., Cottle, J.M., Stearns, M.A., Poletti,
7 J.E., Seward, G.G.E., 2013. Campaign-style titanite U – Pb dating by laser-ablation ICP : Implications for
8 crustal flow , phase transformations and titanite closure. *Chemical Geology* 341, 84–101.
9 doi:10.1016/j.chemgeo.2012.11.012
- 10 Stearns, M.A., Cottle, J.M., Hacker, B.R., Kylander-Clark, A.R.C., 2016. Extracting thermal histories
11 from the near-rim zoning in titanite using coupled U-Pb and trace-element depth profiles by single-shot
12 laser-ablation split stream (SS-LASS) ICP-MS. *Chemical Geology* 422, 13–24.
13 doi:10.1016/j.chemgeo.2015.12.011
- 14 Stearns, M.A., Hacker, B.R., Ratschbacher, L., Rutte, D., Kylander-clark, A.R.C., 2015. Titanite
15 petrochronology of the Pamir gneiss domes: Implications for middle to deep crust exhumation and titanite
16 closure to Pb and Zr diffusion. *Tectonics* 34, 784–802. doi:10.1002/2014TC003774.Received
- 17 Stipska, P., Powell, R., Hacker, B.R., Holder, R., 2016. Uncoupled U / Pb and REE response in zircon
18 during the transformation of eclogite to mafic and intermediate granulite (Blanský les , Bohemian
19 Massif). *Journal of Meta* 34, 551–572. doi:10.1111/jmg.12193
- 20 Storey, C.D., Smith, M.P., Jeffries, T.E., 2007. In situ LA-ICP-MS U – Pb dating of metavolcanics of
21 Norrbotten , Sweden : Records of extended geological histories in complex titanite grains. *Chemical*
22 *Geology* 240, 163–181. doi:10.1016/j.chemgeo.2007.02.004
- 23 Stübner, K., Grujic, D., Parrish, R.R., Roberts, N.M.W., Kronz, A., Wooden, J., Ahmad, T., 2014. Lithos
24 Monazite geochronology unravels the timing of crustal thickening in NW Himalaya. *LITHOS* 210–211,
25 111–128. doi:10.1016/j.lithos.2014.09.024
- 26 Tera, F., Wasserburg, G.J., 1972. U-Th-Pb systematics in three Apollo 14 basalts and the problem of
27 initial Pb in lunar rocks. *Earth and Planetary Science Letters* 14, 281–304. doi:10.1016/0012-
28 821X(72)90128-8
- 29 Terry, M.P., Hamilton, M.A., 2000. Monazite geochronology of UHP and HP metamorphism ,
30 deformation , and exhumation , Nordoyane ... doi:10.2138/am-2000-11-1208
- 31 Tomascak, P.B., Krogstad, E.J., Walker, R.J., 1996. U-Pb Monazite Geochronology of Granitic Rocks
32 from Maine: Implications for Late Paleozoic Tectonics in the Northern Appalachians. *The Journal of*
33 *Geology* 104, 185–195.
- 34 Verts, L.A., Frost, C.D., 1996. U-Pb sphene dating of metamorphism : the importance of sphene growth
35 in the contact aureole of the Red Mountain pluton , Laramie Mountains , Wyoming. *Contributions to*
36 *Mineralogy and Petrology* 125, 186–199.
- 37 Watson, E.B., Yan Liang, 1995. A simple model for sector zoning in slowly grown crystals: implications
38 for growth rate and lattice diffusion, with emphasis on accessory minerals in crustal rocks. *American*
39 *Mineralogist* 80, 1179–1187.
- 40 Whitehouse, M.J., Platt, Æ.J.P., 2003. Dating high-grade metamorphism - constraints from rare-earth
41 elements in zircon and garnet. *Contributions to Mineralogy and Petrology* 145, 61–74.
42 doi:10.1007/s00410-002-0432-z

1 Wieldenbeck, M., Allé, P., Corfú, F., Griffin, W.L., Meier, M., Oberli, F., Quadt, A. Von, Roddick, J.C.,
2 Spiegel, W., 1995. Three Natural Zircon Standards for U-Th-Pb, Lu-Hf, Trace Element and REE
3 Analyses. *Geostandards Newsletter* 19, 1–23. doi:10.1111/j.1751-908X.1995.tb00147.x

4 Williams, M.L., Jercinovic, M.J., Hetherington, C.J., 2007. Microprobe Monazite Geochronology:
5 Understanding Geologic Processes by Integrating Composition and Chronology. *Annual Review of Earth
6 and Planetary Sciences* 35, 137–175. doi:10.1146/annurev.earth.35.031306.140228

7 Zeck, H.P., Wingate, M.T.D., Pooley, G.D., Ugidos, J.M., 2004. A Sequence of Pan-African and
8 Hercynian Events Recorded in Zircons from an Orthogneiss from the Hercynian Belt of Western Central
9 Iberia —an Ion Microprobe U– Pb Study 45, 1613–1629. doi:10.1093/petrology/egh026

10 Zeringue, J., Bowring, J.~F., McLean, N.~M., Pastor, F., 2014. Building Interactive Visualizations for
11 Geochronological Data. AGU Fall Meeting Abstracts.

12 Zhu, X.K., O’Nions, R.K., Belshaw, N.S., Gibb, A.J., 1997. Significance of in situ SIMS chronometry of
13 zoned monazite from the Lewisian granulites, northwest Scotland. *Chemical Geology* 5, 35–53.

14
15
16
17
18
19
20
21
22
23
24
25
26
27
28
29
30
31
32
33
34
35
36
37
38

1 FIGURE CAPTIONS

2 Figure 1. Geological map of the study area and location of the samples, modified from Arenas and
3 Martínez Catalán (2002): (a) Location of the Órdenes complex within the Iberian massif. (b) Sobrado
4 Unit map, indicating units and horses. (c) Cross-section in WNW-ESE direction and (d) SW-NE and
5 SSW-NNE direction of the Sobrado antiform. Sample location are indicated.

6 Figure 2. Cathodoluminescence (CL) images with the location of the analyzed spots for selected zircon
7 grains.

8 Figure 3. (a) Tera-Wasserburg diagram showing distribution of analysed titanites (n = 51) from Sobrado
9 amphibolite (JBP-71-21). The rejected analyses are represented by gray ellipses. The ellipses represent
10 the $^{207}\text{Pb}/^{206}\text{Pb}$ and $^{238}\text{U}/^{206}\text{Pb}$ errors ($\pm 2\sigma$). (b) Chondrite-normalized rare earth element (REE) patterns
11 for the same titanites.

12 Figure 4. (a) Monazite grain compositional maps in paragneiss with a 30% thorium variation. Location
13 and spot numbers (46 and 47) are indicated, as well as the $^{206}\text{Pb}/^{238}\text{U}$ age and error ($\pm 2\sigma$). (b) Chondrite-
14 normalized rare earth element (REE) patterns for the same monazites in (a).

15 Figure 5. (a) Tera-Wasserburg diagram showing distribution of analysed monazites (n = 76) from
16 Sobrado paragneiss (JBP-71-15). The rejected analyses are represented by gray ellipses. The ellipses
17 represent the $^{207}\text{Pb}/^{206}\text{Pb}$ and $^{238}\text{U}/^{206}\text{Pb}$ errors ($\pm 2\sigma$). (b) Chondrite-normalized rare earth element (REE)
18 patterns for the same monazites.

19 Figure 6. Concordia plot (a) including all zircon with concordance >90% from sample JBP-71-15
20 (Sobrado migmatitic paragneiss), and (b) age histogram and probability density plot for ages older than
21 1000 Ma.

22 Figure 7. Tera-Wasserburg diagram (a) for the analyses between 589 and 380 Ma, and, (b) age histogram
23 and probability density plot for the same ages.

24 Figure 8. Th/U ratio versus $^{206}\text{Pb}/^{238}\text{U}$ ages for the zircon analyses from 589 to 380 Ma. Analysis 63 (510
25 Ma) is not represented as it has an anomalous value (6.59).

26 Figure 9. Weighed average obtained from magmatic ages distributed between 589 and 510 Ma.

27 Figure 10. Chondrite-normalized plots for (a) inherited zircon older than 1000 Ma, and (b) zircon
28 between 589 and 380 Ma.

29 Figure 11. (a) Hafnium versus age, (b) Yb/Gd versus age, (c) Eu/Eu* versus age, and (d) U/Ce versus Th
30 for zircon analyses between 589 and 380 Ma.

31 Figure 12. Age of the onset of the oldest HP-HT metamorphic event obtained using the TuffZirc
32 algorithm.

33

34 Table 1: U-Th_Pb+REE Titanite_McD_S

35 Table 2A: U-Th_Pb+REE Monazite_McD_S

36 Table 3: U-Th_Pb Zircon sorted by age

37 Table 4A: REE Zircon_McD_S sorted by age

38 Table 4B: REE Zircon_McD_S sorted by age

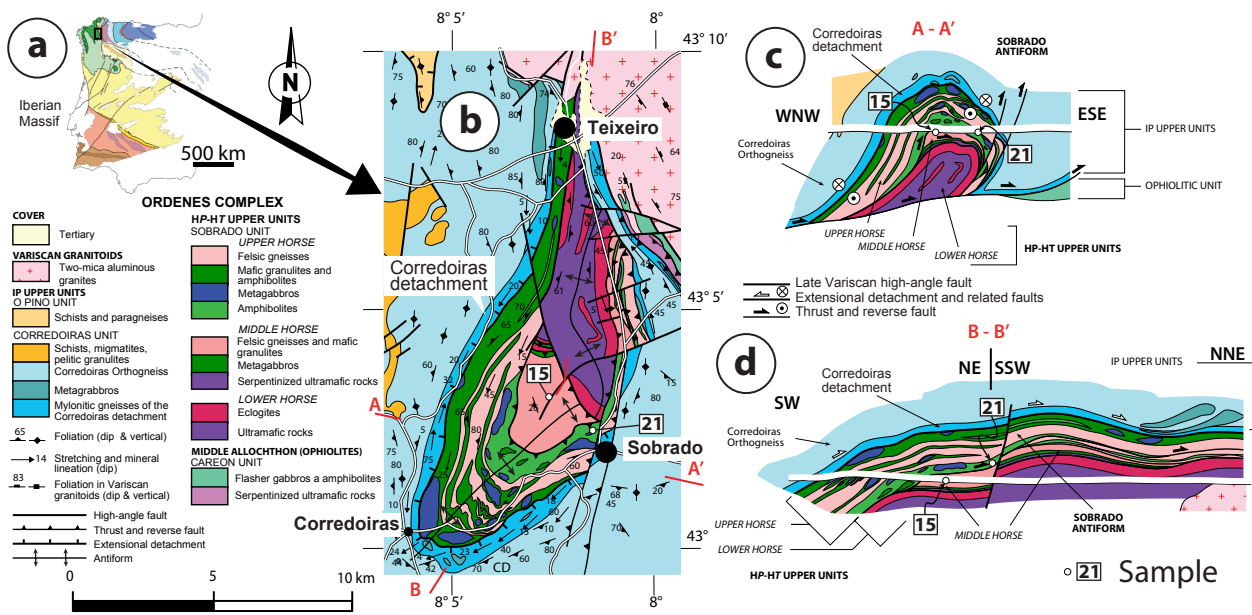
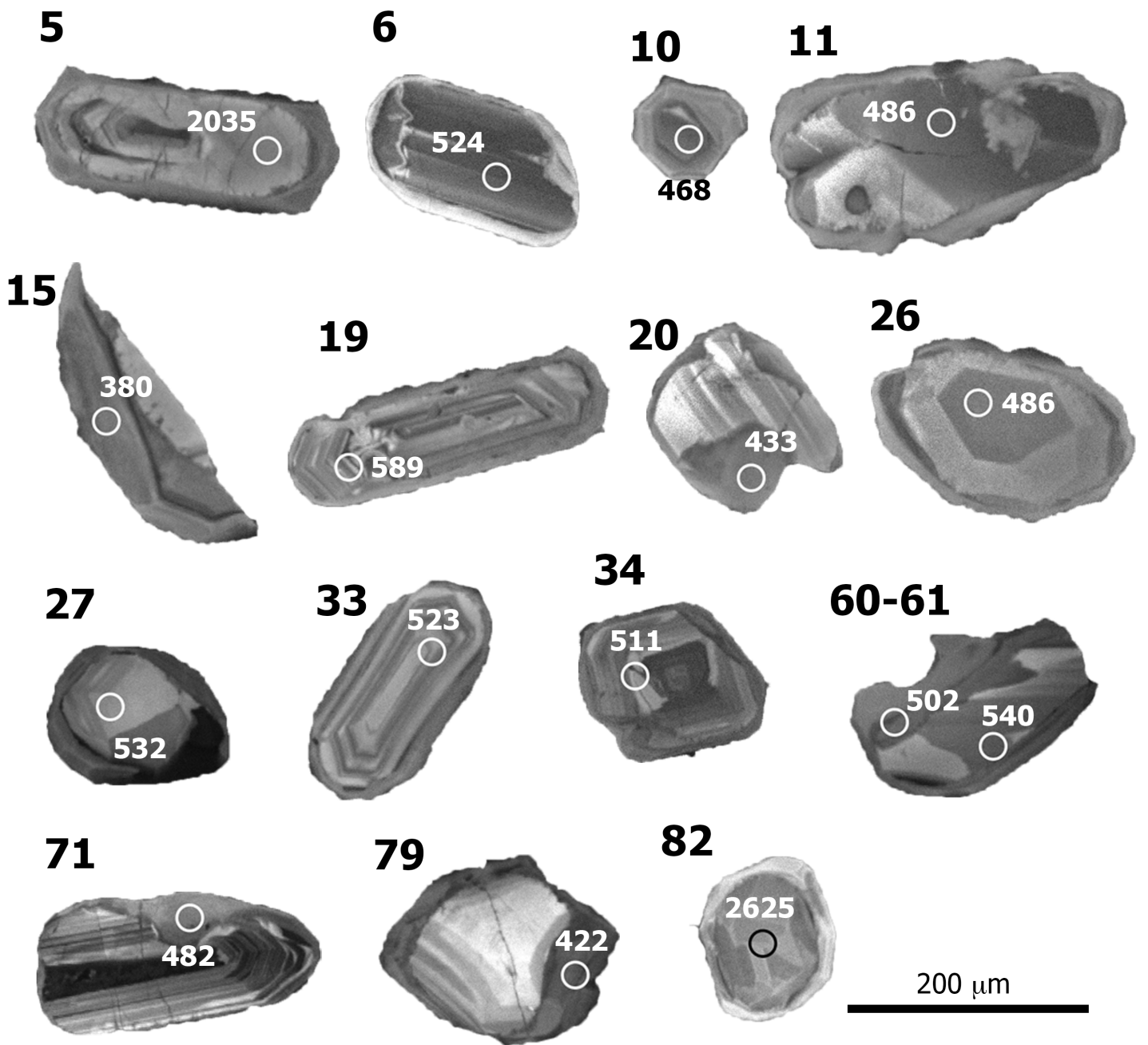


Figure 1. Geological map of the study area and location of the samples, modified from Arenas and Martínez Catalán (2002): (a) Location of the Ordenes complex within the Iberian massif. (b) Sobrado Unit map, indicating units and horses. (c) Cross-section in WNW-ESE direction and (d) SW-NE and SSW-NNE direction of the Sobrado antiform. Sample location are indicated.

Figure 2



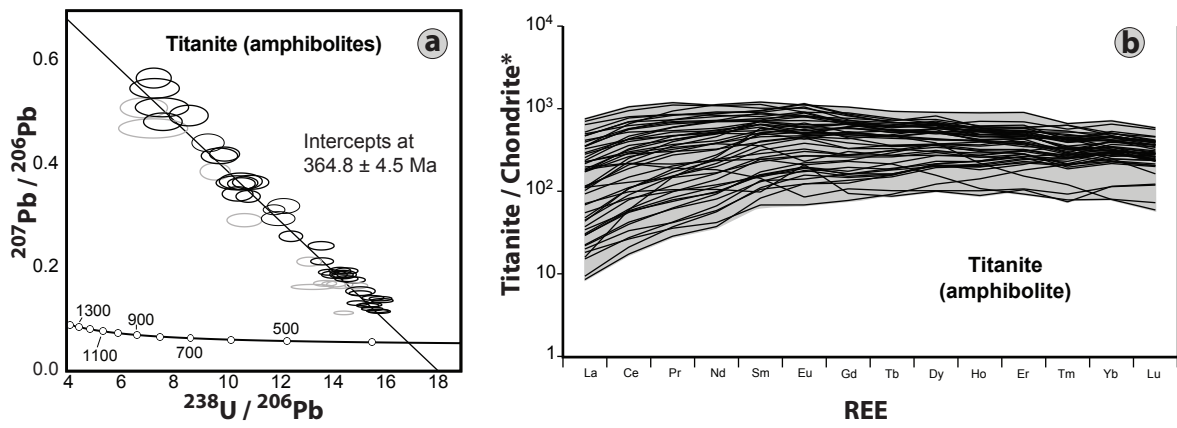


Figure 3. (a) Tera-Wasserburg diagram showing distribution of analysed titanites ($n = 51$) from Sobrado amphibolite (JBP-71-21). The rejected analyses are represented by gray ellipses. The ellipses represent the $^{207}\text{Pb}/^{206}\text{Pb}$ and $^{238}\text{U}/^{206}\text{Pb}$ errors ($\pm 2\sigma$). (b) Chondrite-normalized rare earth element (REE) patterns for the same titanites.

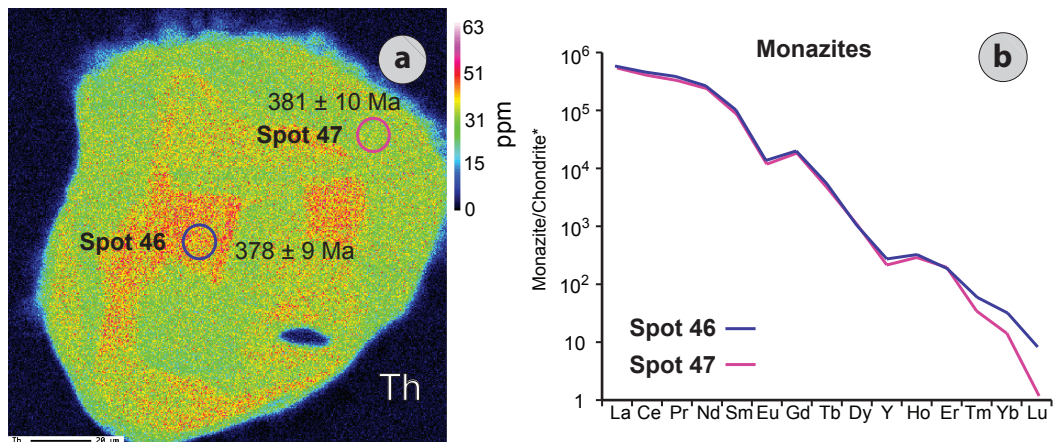


Figure 4. (a) Monazite grain compositional maps in paragneiss with a 30% thorium variation. Location and spot numbers (46 and 47) are indicated, as well as the $^{206}\text{Pb}/^{238}\text{U}$ age and error ($\pm 2\sigma$). (b) Chondrite-normalized rare earth element (REE) patterns for the same monazites in (a).

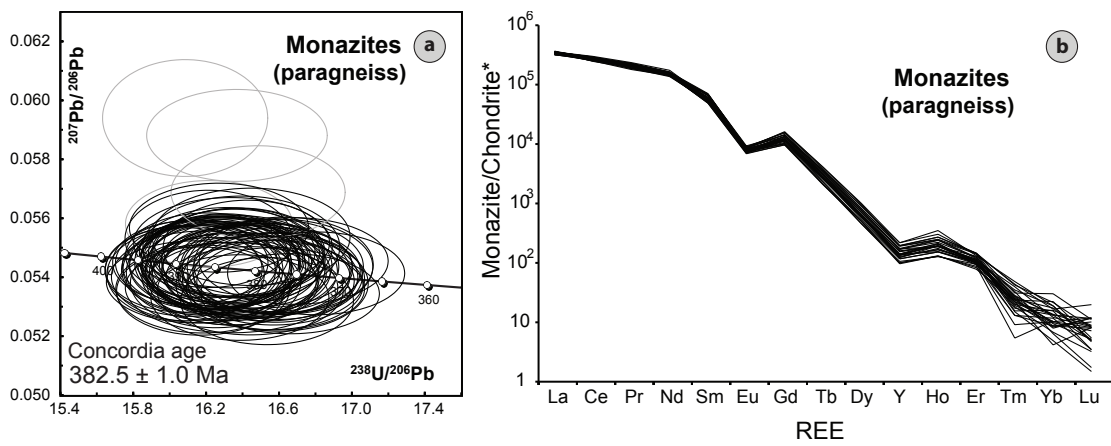
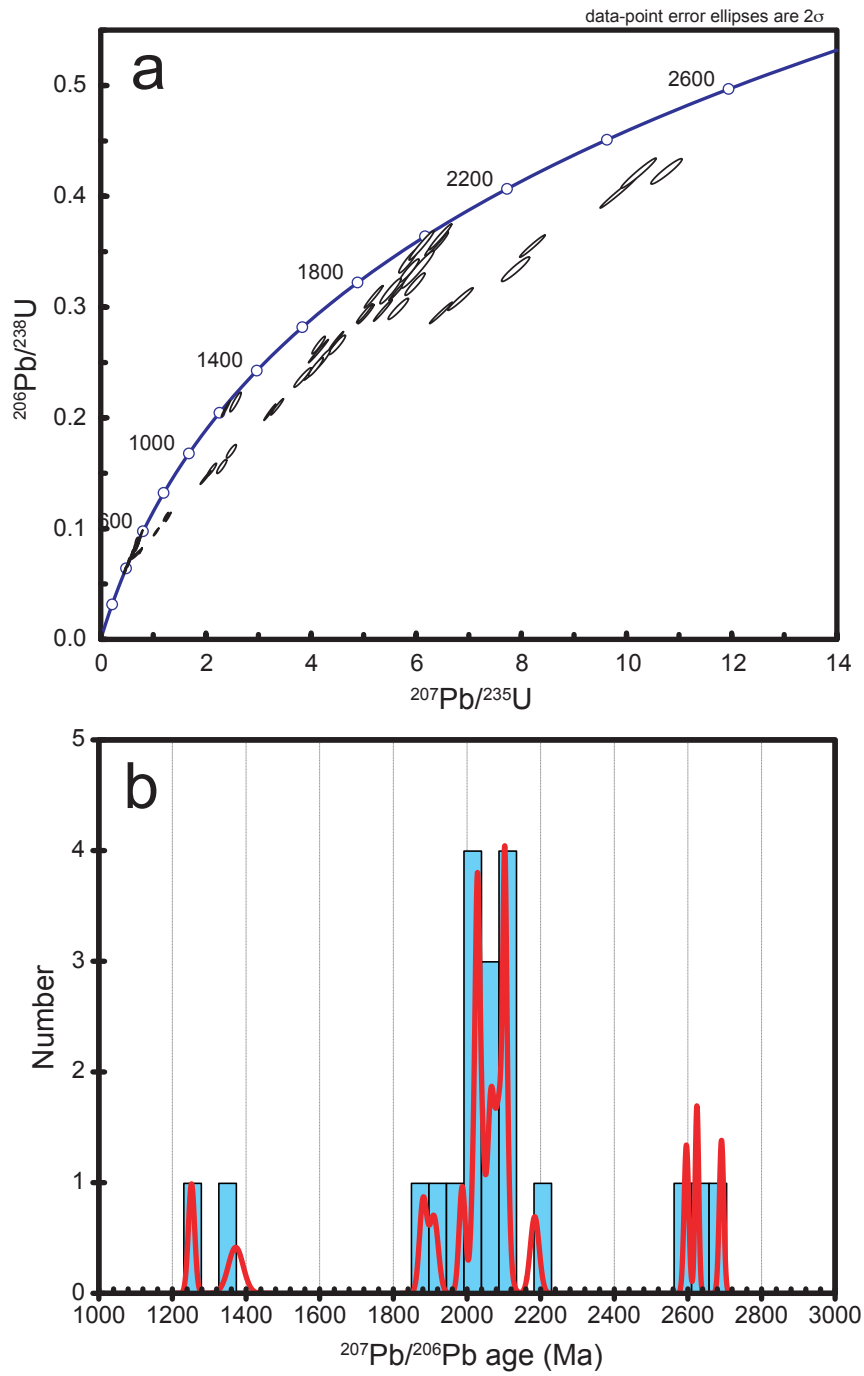
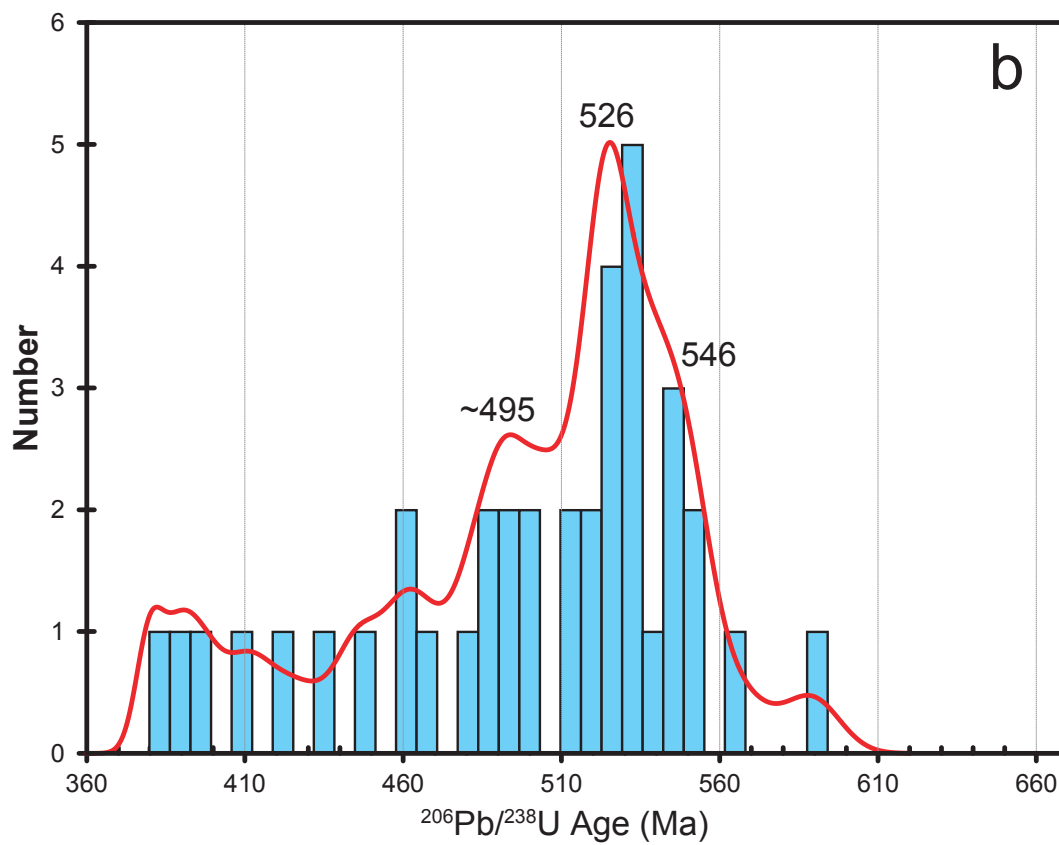
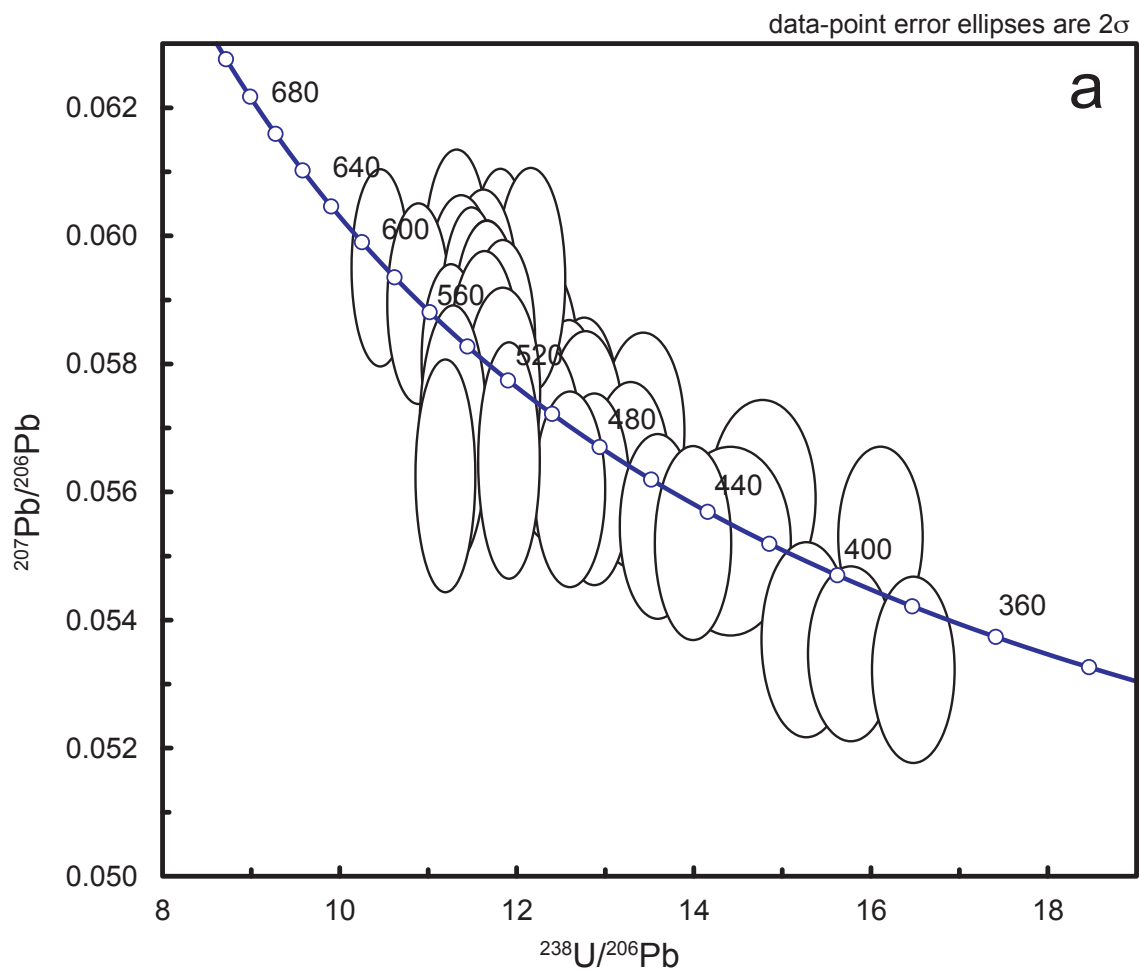
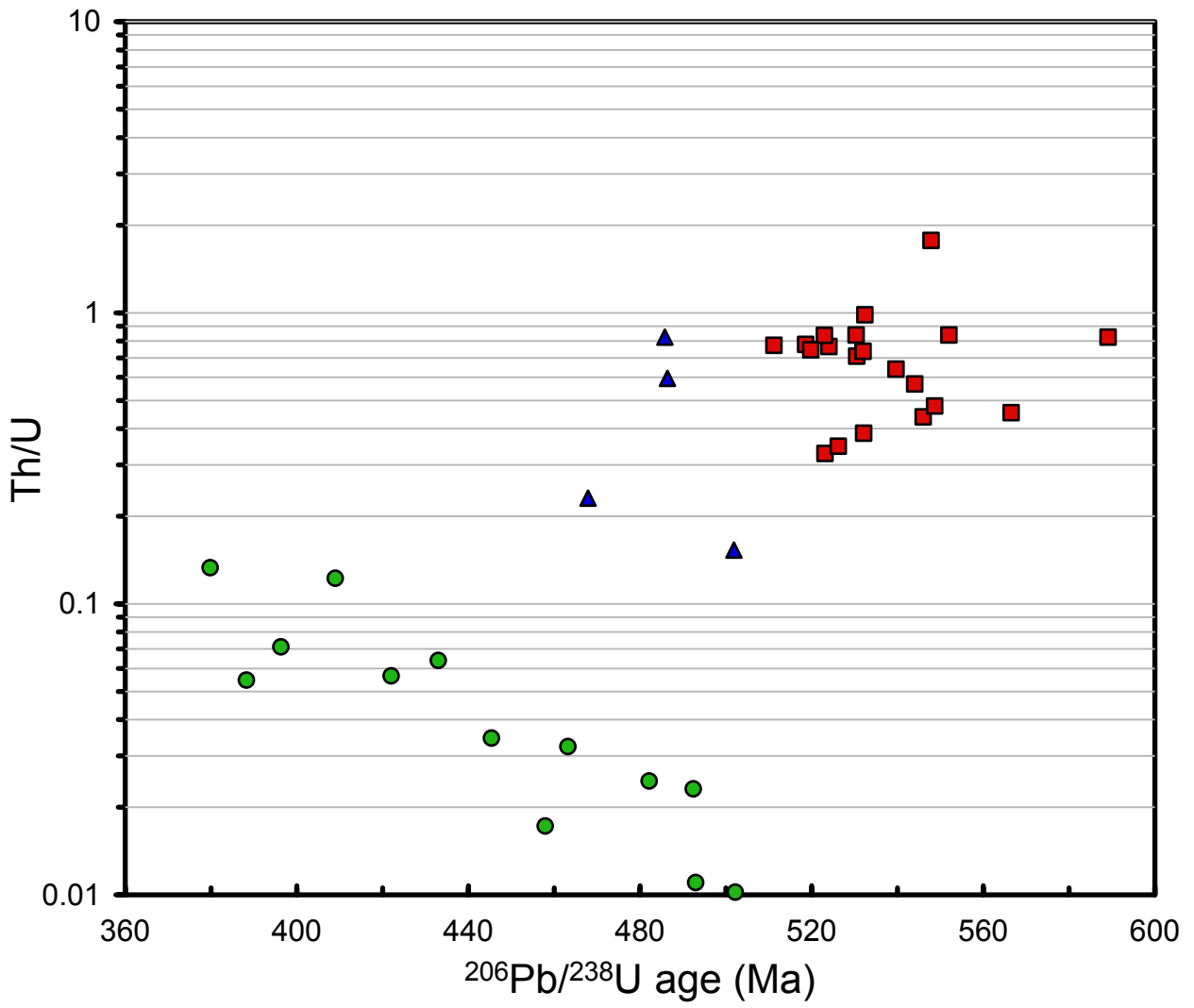


Figure 5. (a) Tera-Wasserburg diagram showing distribution of analysed monazites ($n = 76$) from Sobrado paragneiss (*JBP-71-15*). The rejected analyses are represented by gray ellipses. The ellipses represent the $^{207}\text{Pb}/^{206}\text{Pb}$ and $^{238}\text{U}/^{206}\text{Pb}$ errors ($\pm 2\sigma$). (b) Chondrite-normalized rare earth element (REE) patterns for the same monazites.







box heights are 2σ

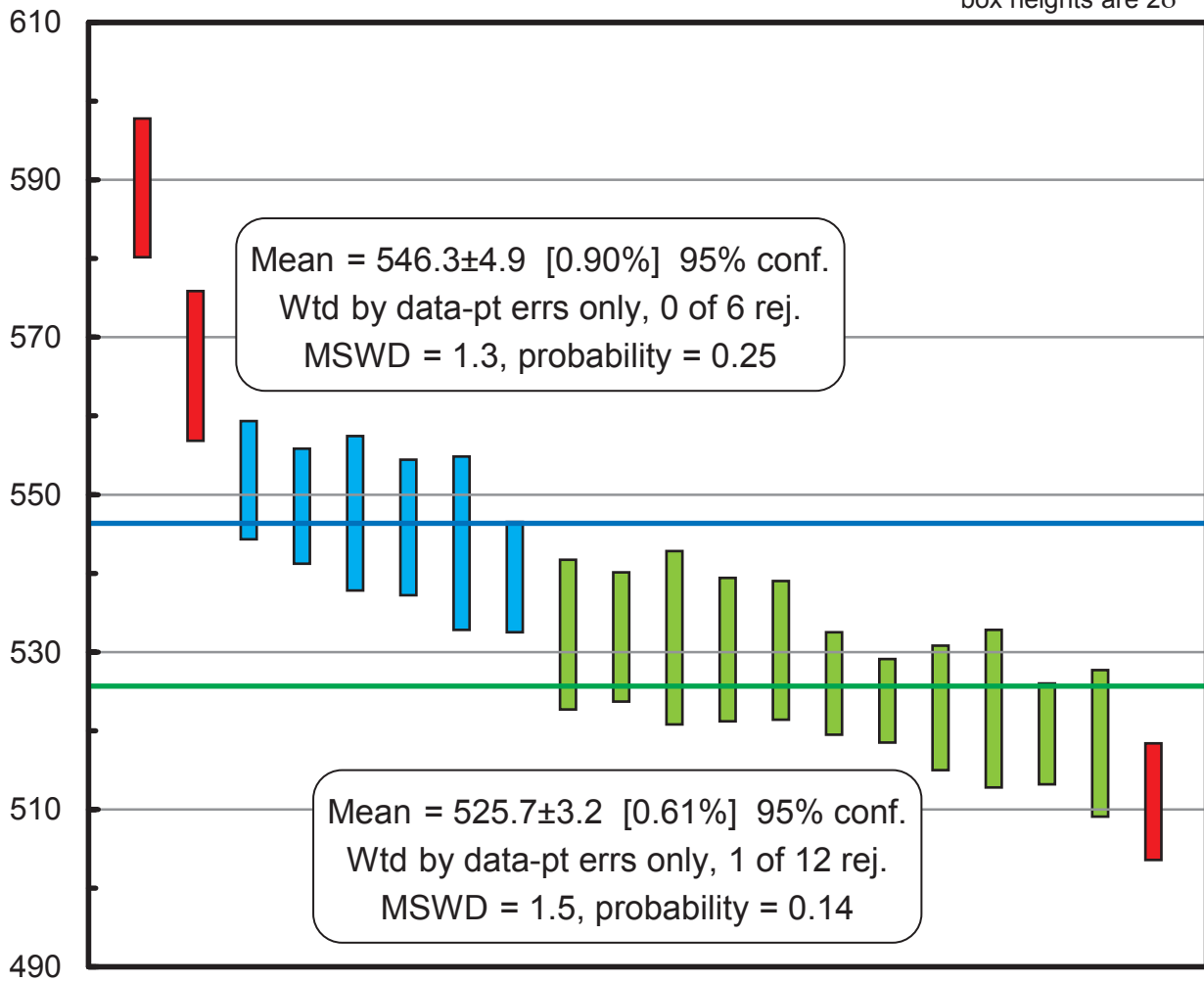


Figure 10b

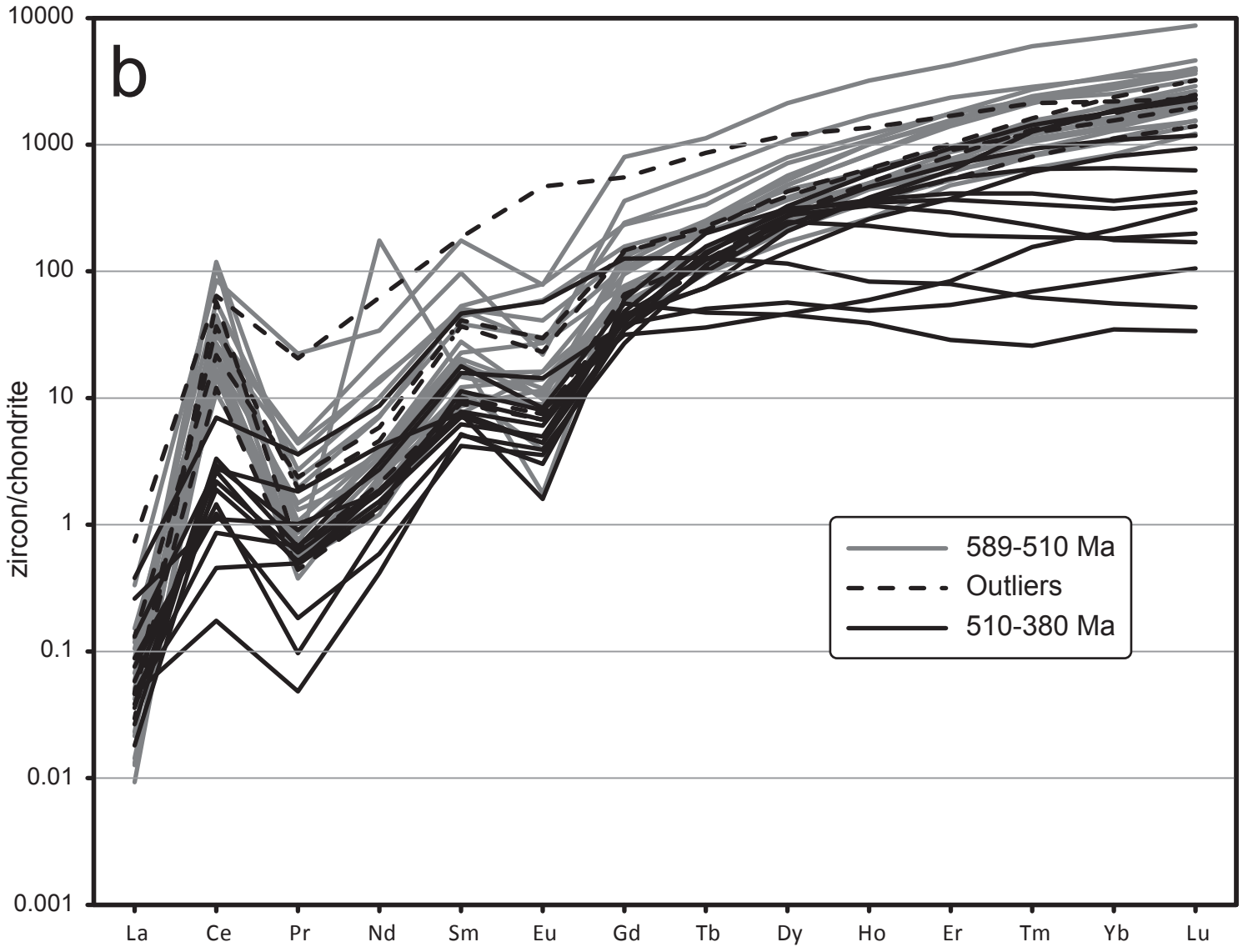
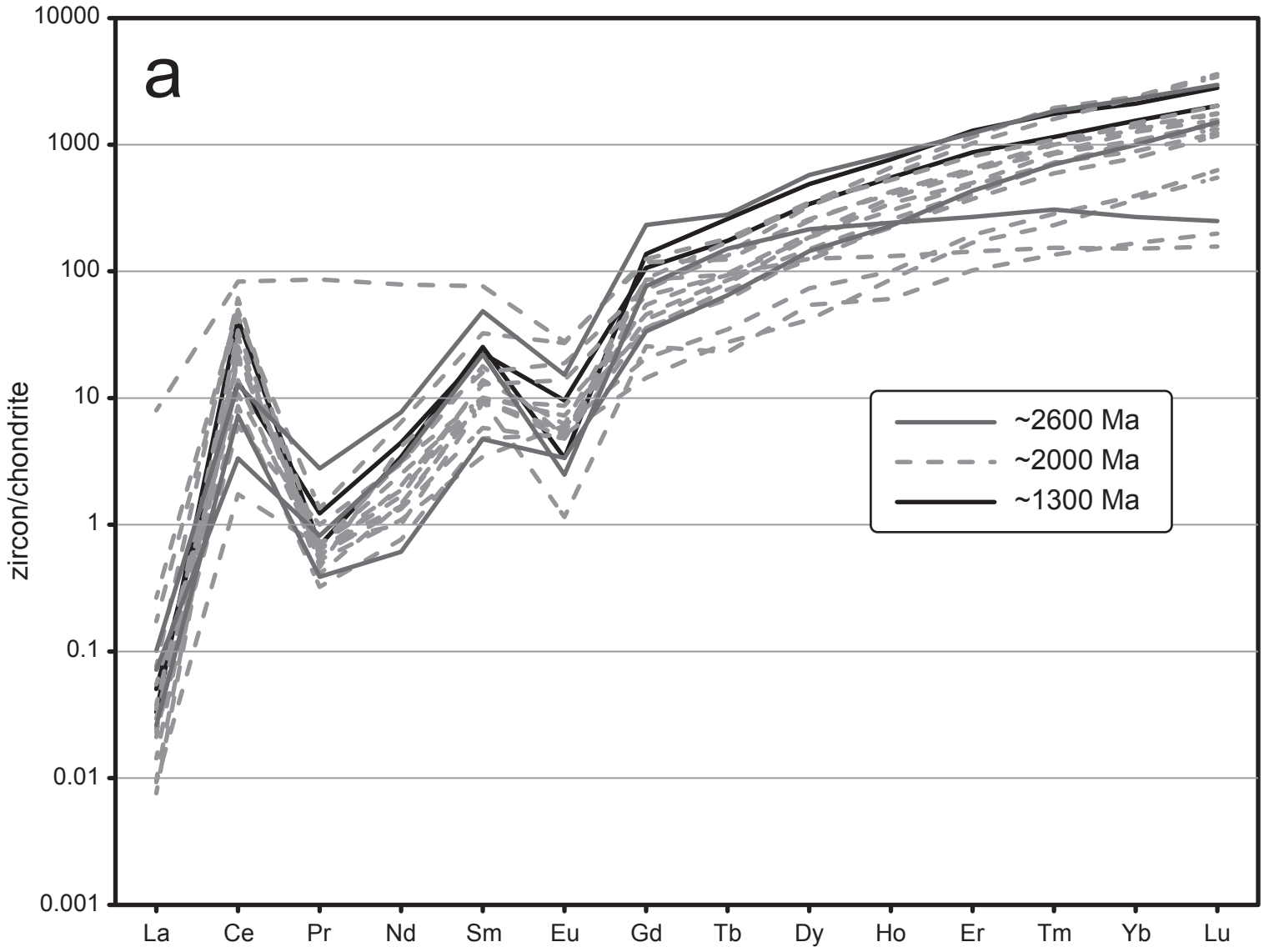


Figure 10a



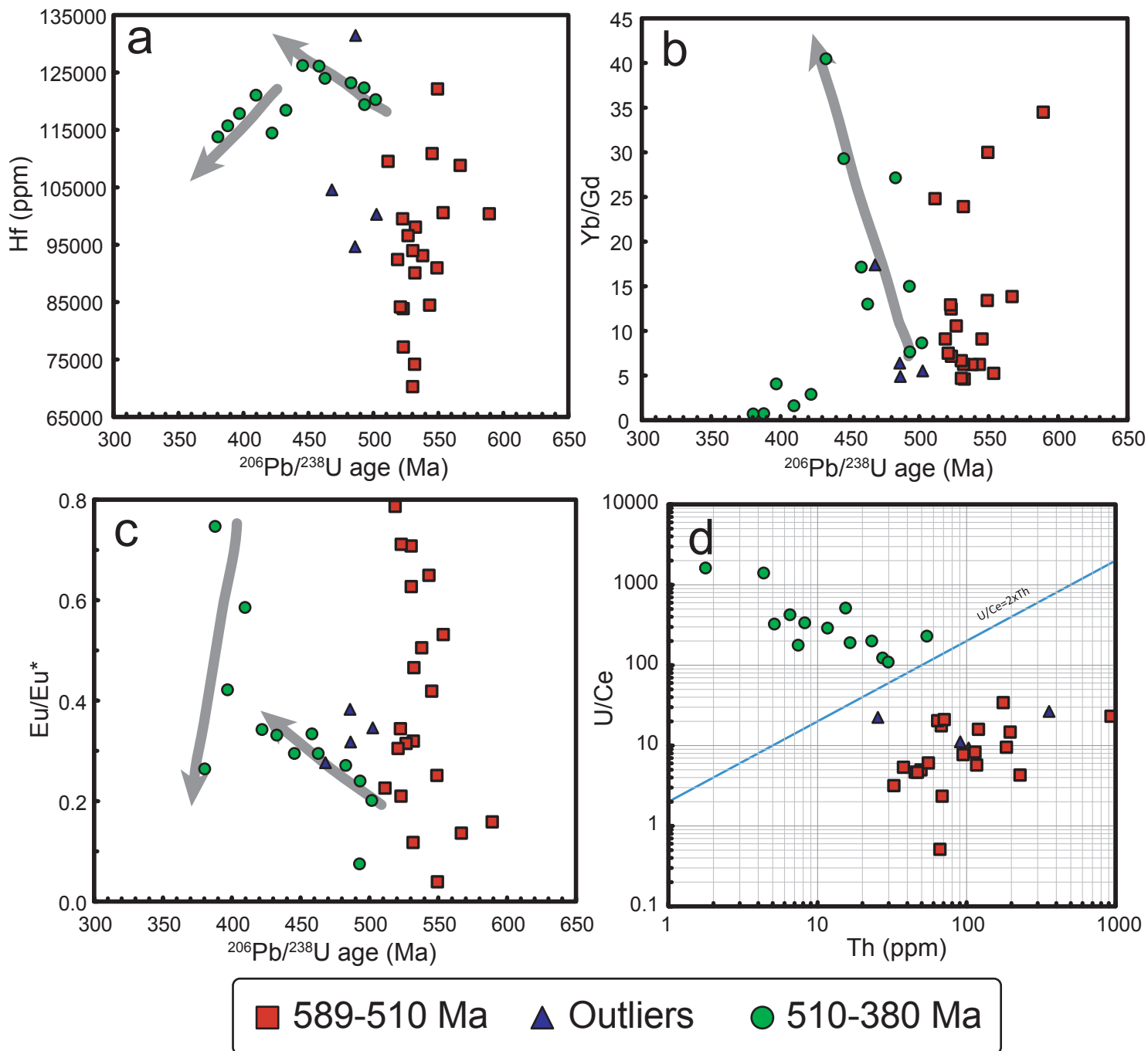


Table 1_U-Th_Pb+REE Titatine_McD_s

Spot	²³⁸ U/ppm	²³⁵ U/ ²³⁸ U	²⁰⁷ Pb/ ²⁰⁶ Pb	²⁰⁶ Pb/ ²³⁸ U	U (ppm)	Th (ppm)	La (ppm)	Ce (ppm)	Pr (ppm)	Nd (ppm)	Sm (ppm)	Eu (ppm)	Gd (ppm)	Tb (ppm)	Dy (ppm)	Ho (ppm)	Er (ppm)	Tm (ppm)	Yb (ppm)	Lu (ppm)	
1	15.59 ± 0.35	0.1279 ± 0.0032	0.02292 ± 0.00053	0.02580 ± 0.00074	7.42	16.57	75.1	1052	1182	1096	1012	1012	818	681	635	590	521	423.1	405	363.4	
2	13.37 ± 0.66	0.1625 ± 0.0040	0.02580 ± 0.00074	0.03513 ± 0.00101	8.22	16.73	701	946	1107	1085	1128	908	889	762	661	584	483	333.6	324	232.9	
3	13.74 ± 0.36	0.2123 ± 0.0056	0.03513 ± 0.00101	0.05140 ± 0.00298	4.16	7.44	327	424	520	538	650	588	574	559	522	411.7	465	411.7	465	392.7	
4	13.95 ± 0.36	0.1694 ± 0.0045	0.05140 ± 0.00298	0.05450 ± 0.00376	4.30	2.47	116	188	275	318	484	519	503	471	419	408	365	278.9	299	230.5	
5	13.70 ± 0.41	0.2426 ± 0.0067	0.05450 ± 0.00376	0.03180 ± 0.00119	2.71	2.35	109	209	297	383	511	561	458	437	422	416	386	287.9	315	261.4	
6	14.20 ± 0.40	0.1864 ± 0.0058	0.03180 ± 0.00119	0.15000 ± 0.01111	3.16	4.74	225	300	369	409	547	671	515	539	495	526	511	393.5	448	383.7	
7	12.06 ± 0.52	0.2955 ± 0.0111	0.15000 ± 0.01111	0.03051 ± 0.00091	2.00	1.46	68	111	153	199	314	382	329	361	373	394	399	318.6	340	290.7	
8	14.52 ± 0.33	0.1863 ± 0.0050	0.03051 ± 0.00091	0.02719 ± 0.00074	4.86	7.93	394	574	681	705	762	813	685	648	589	608	579	438.8	504	417.1	
9	15.11 ± 0.35	0.1310 ± 0.0037	0.02719 ± 0.00074	0.14400 ± 0.00410	6.55	10.39	471	692	733	803	861	828	714	679	636	703	693	565.6	650	561.0	
10	12.55 ± 0.37	0.2611 ± 0.0083	0.14400 ± 0.00410	0.03340 ± 0.00137	2.35	0.96	45	90	152	217	359	442	328	328	300	291	304	252.6	290	245.5	
11	15.48 ± 0.35	0.1264 ± 0.0034	0.03340 ± 0.00137	0.07200 ± 0.00601	8.13	6.22	350	654	938	1120	1201	1107	1045	928	902	890	901	659.9	711	586.6	
12	7.30 ± 1.08	0.4710 ± 0.0153	0.07200 ± 0.00601	0.11200 ± 0.00503	0.61	0.32	15	27	42	67	134	140	162	189	215	233	264	248.2	287	232.1	
13	10.02 ± 0.47	0.4211 ± 0.0111	0.11200 ± 0.00503	0.22000 ± 0.01706	1.20	0.69	31	61	98	139	244	209	230	214	156	108	93	78.5	80	72.8	
14	9.66 ± 0.47	0.3870 ± 0.0115	0.22000 ± 0.01706	0.03377 ± 0.00107	1.09	0.56	29	55	79	96	159	197	160	181	200	213	249	230.4	296	242.7	
15	13.99 ± 0.32	0.1910 ± 0.0046	0.03377 ± 0.00107	0.13000 ± 0.03609	4.58	6.10	184	317	421	512	599	485	518	467	433	401	374	319.8	306	236.2	
16	14.41 ± 0.41	0.1672 ± 0.0063	0.03150 ± 0.00144	0.08000 ± 0.00600	4.02	5.44	216	359	421	492	642	501	609	609	590	549	545	471.3	464	395.9	
17	14.94 ± 0.36	0.1761 ± 0.0048	0.13000 ± 0.03609	0.05140 ± 0.00216	4.38	0.71	43	108	170	239	404	460	433	485	572	540	536	488.3	420	339.0	
18	7.35 ± 0.77	0.5490 ± 0.0155	-0.08000 ± 0.00600	0.05140 ± 0.00216	0.55	0.30	18	26	36	42	68	68	77	92	122	141	181	210.9	230	204.5	
19	15.96 ± 0.36	0.1397 ± 0.0034	0.02710 ± 0.00071	0.05770 ± 0.00542	8.10	9.22	414	520	541	580	692	609	652	624	708	579	591	630.8	507	405.7	
20	15.04 ± 0.36	0.1649 ± 0.0049	0.03031 ± 0.00096	0.03279 ± 0.00098	6.39	8.79	293	426	468	522	543	499	482	455	514	419	438	446.6	412	321.1	
21	11.90 ± 0.34	0.3127 ± 0.0079	0.37000 ± 0.02202	0.03350 ± 0.00183	2.91	0.40	48	108	185	276	507	426	527	465	385	218	153	120.2	80	59.3	
22	14.41 ± 0.34	0.1940 ± 0.0054	0.05140 ± 0.00216	0.09800 ± 0.01612	5.29	3.73	255	465	598	716	889	794	766	709	817	603	595	628.1	472	382.1	
23	14.18 ± 0.37	0.1682 ± 0.0046	0.09800 ± 0.01612	0.05840 ± 0.00378	4.77	1.43	102	228	355	458	710	718	697	604	671	488	476	449.4	344	258.5	
24	15.92 ± 0.35	0.1147 ± 0.0030	0.02388 ± 0.00057	0.12200 ± 0.00542	10.78	13.20	468	695	829	915	901	1052	731	604	620	458	442	428.3	323	278.0	
25	7.67 ± 0.83	0.5120 ± 0.0150	-0.03000 ± 0.00400	0.05770 ± 0.00542	0.68	0.17	9	21	37	56	110	157	147	157	209	182	211	270.4	234	214.2	
26	12.23 ± 0.50	0.3200 ± 0.0119	0.05770 ± 0.00542	0.03279 ± 0.00098	1.68	2.17	93	148	203	243	286	325	275	274	313	271	307	349.0	312	285.4	
27	14.67 ± 0.35	0.1937 ± 0.0048	0.03279 ± 0.00098	0.03350 ± 0.00183	4.67	6.77	354	560	653	700	703	639	652	551	557	401	347	332.8	248	162.6	
28	15.20 ± 0.46	0.1543 ± 0.0069	0.03350 ± 0.00183	0.02158 ± 0.00049	4.88	4.43	174	326	463	554	642	542	593	512	581	487	521	521.1	496	453.7	
29	14.56 ± 0.31	0.1120 ± 0.0029	0.02158 ± 0.00049	0.05840 ± 0.00378	11.71	22.45	495	625	696	722	728	886	653	584	642	562	575	536.0	444	363.0	
30	10.92 ± 0.38	0.3387 ± 0.0094	0.05840 ± 0.00378	0.12200 ± 0.00542	1.54	2.51	111	129	147	168	228	228	228	270	312	375	364	431	455.9	451	411.0
31	10.64 ± 0.67	0.3680 ± 0.0132	0.12200 ± 0.00542	0.09500 ± 0.00969	1.07	0.81	29	58	84	114	158	173	195	184	230	228	262	283.0	270	259.3	
32	9.39 ± 0.50	0.4430 ± 0.0141	-0.02000 ± 0.00400	0.09500 ± 0.00969	0.90	0.58	22	42	61	81	130	179	152	162	207	205	242	246.2	289	248.8	
33	10.49 ± 0.65	0.3651 ± 0.0111	0.09500 ± 0.00969	0.04200 ± 0.00378	1.13	1.22	55	82	100	120	149	189	163	162	203	196	229	210.5	247	236.6	
34	15.19 ± 0.35	0.1501 ± 0.0040	0.04200 ± 0.00378	0.03390 ± 0.00129	5.56	3.48	235	434	593	696	705	801	639	537	517	454	488	390.3	419	399.2	
35	14.53 ± 0.41	0.1866 ± 0.0067	0.03390 ± 0.00129	0.03390 ± 0.00129	3.69	4.89	172	283	322	383	457	471	483	465	516	482	494	401.6	464	401.2	
36	14.66 ± 0.36	0.1785 ± 0.0047	0.05840 ± 0.00378	0.05840 ± 0.00378	4.36	2.21	111	252	399	514	703	588	649	544	524	463	461	351.8	391	368.3	
37	16.03 ± 0.34	0.1359 ± 0.0032	0.04720 ± 0.00230	0.04720 ± 0.00230	8.41	3.38	281	400	473	503	493	611	443	355	366	321	320	264.8	297	287.8	
38	10.52 ± 0.48	0.3435 ± 0.0113	0.14400 ± 0.00600	0.14400 ± 0.00600	1.28	0.55	22	40	63	93	172	221	236	293	370	352	385	304.0	348	308.1	
39	8.65 ± 0.61	0.4960 ± 0.0164	0.00000 ± 0.00000	0.00000 ± 0.00000	0.66	0.24	9	17	29	37	83	123	126	158	158	215	232	284	215.8	278	267.9
40	15.85 ± 0.34	0.1160 ± 0.0028	0.02681 ± 0.00080	0.02681 ± 0.00080	7.59	7.20	348	566	735	869	950	1151	862	731	739	619	632	420.2	530	460.6	
41	11.89 ± 0.31	0.1654 ± 0.0046	0.06000 ± 0.01400	0.06000 ± 0.01400	2.54	0.09	16	60	148	259	580	512	595	518	511	425	428	291.9	411	362.2	
42	9.82 ± 0.57	0.4175 ± 0.0124	0.13800 ± 0.03205	0.13800 ± 0.03205	0.95	0.79	71	99	105	105	98	210	94	87	100	89	104	74.5	115	122.0	
43	15.67 ± 0.34	0.1411 ± 0.0037	0.02576 ± 0.00068	0.02576 ± 0.00068	6.21	10.38	640	799	852	832	803	913	671	607	625	520	493	319.8	397	362.2	
44	11.01 ± 0.57	0.3661 ± 0.0111	0.11000 ± 0.04002	0.11000 ± 0.04002	1.50	0.86	34	57	75	99	154	196	174	174	218	274	274	316	272.5	369	345.9
45	7.67 ± 0.60	0.4840 ± 0.0139	0.04000 ± 0.02500	0.04000 ± 0.02500	0.57	0.33	20	33	42	58	105	123	136	150	193	200	221	204.0	263	280.5	
46	13.25 ± 0.39	0.2117 ± 0.0071	0.03790 ± 0.00242	0.03790 ± 0.00242	2.61	4.41	228	284	304	324	395	455	384	348	358	302	284	195.5	227	204.9	
47	10.78 ± 0.54	0.2924 ± 0.0105	0.13300 ± 0.07405	0.13300 ± 0.07405	1.66	0.79	37	79	118	165	255	304	277	309	340	313	321	253.8	305	288.2	
48	6.94 ± 0.74	0.5110 ± 0.0158	0.07450 ± 0.00570	0.07450 ± 0.00570	0.64	1.89	173	290	339	376	356	330	303	269	273	260	255	186.6	217	199.2	
49	15.64 ± 0.33	0.1197 ± 0.0028	0.03214 ± 0.00100	0.03214 ± 0.00100	10.32	7.50	521	772	845	886	937	1130	839	676	683	551	478	336.0	339	299.2	
50	10.66 ± 0.43	0.3635 ± 0.0094	0.06970 ± 0.00481	0.06970 ± 0.00481	1.77	2.45	197	218	215	235	245	269	259	259	294	258	279	210.9	246	236.6	
51	7.32 ± 0.55	0.5690 ± 0.0158	0.08940 ± 0.00820	0.08940 ± 0.00820	0.70	1.76	183	217	191	182	143	85	107	102	102	101	107	92.3	114	118.7	

Table 2A_U-Th_Pb+REE Monazite_McD_S

Spot	²³⁸ U/ ²⁰⁶ Pb	²⁰⁷ Pb/ ²⁰⁶ Pb	²⁰⁸ Pb/ ²³² Th	U (ppm)	Th (ppm)	La (ppm)	Ce (ppm)	Pr (ppm)	Nd (ppm)	Sm (ppm)	Eu (ppm)	Gd (ppm)	Tb (ppm)	Dy (ppm)	Y (ppm)	Ho (ppm)	Er (ppm)	Tm (ppm)	Yb (ppm)	Lu (ppm)	
1	16.29 ± 0.35	0.0543 ± 0.0013	0.01930 ± 0.00041	1640	26200	554430	433931	365302	243932	98243	12131	19899	4429	1082	243	273	170	32.4	20	3.3	
2	16.28 ± 0.35	0.0545 ± 0.0013	0.01916 ± 0.00042	1850	29300	527004	437194	352371	242451	107905	13286	19749	18749	981	272	322	191	27.5	25	0.0	
3	16.20 ± 0.38	0.0544 ± 0.0012	0.01949 ± 0.00044	2300	25500	519409	420881	346983	250109	107905	12451	23869	5319	1163	282	374	190	71.7	8	24.8	
4	16.30 ± 0.38	0.0546 ± 0.0013	0.01930 ± 0.00043	1484	34200	563713	425775	323276	236352	85270	11474	18543	4266	959	192	251	118	46.6	6	12.2	
5	16.18 ± 0.36	0.0543 ± 0.0012	0.01926 ± 0.00043	1805	32400	547257	420881	353448	231947	92568	11385	19899	4197	988	179	260	143	38.1	14	0.0	
6	16.09 ± 0.35	0.0541 ± 0.0012	0.01946 ± 0.00044	1660	25900	524430	402688	338362	230874	96622	11794	19045	4634	1040	227	291	184	44.5	19	5.7	
7	16.27 ± 0.36	0.0544 ± 0.0012	0.01938 ± 0.00044	1790	29000	554430	442968	369612	230853	96676	12647	19598	4072	1045	248	310	172	46.6	20	30.5	
8	16.15 ± 0.36	0.0545 ± 0.0012	0.01920 ± 0.00043	2170	44100	579325	437194	345914	248796	97838	13179	18693	3875	927	203	306	182	42.1	12	8.1	
9	16.22 ± 0.37	0.0558 ± 0.0012	0.01900 ± 0.00042	2150	47100	567511	422512	340517	245295	90608	12451	17789	3958	902	232	286	179	52.2	6	25.6	
10	16.38 ± 0.38	0.0549 ± 0.0012	0.01940 ± 0.00045	1680	27900	526160	435563	357759	242451	93919	12664	19799	4078	947	210	284	143	46.2	11	8.9	
11	16.20 ± 0.37	0.0547 ± 0.0012	0.01930 ± 0.00044	1950	35700	555274	433931	363621	254923	95270	12080	19296	4432	986	221	321	181	44.1	17	5.7	
12	16.29 ± 0.37	0.0546 ± 0.0012	0.01915 ± 0.00044	2280	32800	555274	415997	336207	252298	103176	13215	20201	4510	976	236	280	195	39.7	7	0.0	
13	16.35 ± 0.38	0.0548 ± 0.0012	0.01897 ± 0.00044	2230	43200	540928	411093	349138	246827	94662	12202	18643	4511	976	218	282	138	36.0	13	0.0	
14	16.28 ± 0.36	0.0545 ± 0.0012	0.01908 ± 0.00043	2060	41000	564135	438825	362069	230197	95608	12575	19296	4269	866	209	251	162	16.2	13	11.8	
15	16.31 ± 0.39	0.0545 ± 0.0012	0.01920 ± 0.00043	2020	29600	535865	450245	378233	242888	109932	13268	22412	5125	1085	264	335	179	56.7	16	8.1	
16	16.23 ± 0.36	0.0544 ± 0.0012	0.01953 ± 0.00044	1714	31400	562447	460033	391164	261050	103514	13748	19196	4432	988	211	244	182	37.2	14	12.2	
17	16.40 ± 0.36	0.0546 ± 0.0012	0.01910 ± 0.00045	2360	37500	565401	429038	366379	241357	96689	12388	18894	4352	1004	218	291	177	25.5	10	8.9	
18	16.22 ± 0.36	0.0545 ± 0.0012	0.01943 ± 0.00043	1662	30800	564927	464927	376078	262363	100000	12286	18894	4654	1081	228	308	168	48.2	17	3.3	
19	16.25 ± 0.38	0.0538 ± 0.0013	0.01932 ± 0.00046	1600	31200	518143	442098	363821	244420	101419	12593	20050	4399	1024	217	253	161	34.0	4	2.8	
20	16.11 ± 0.35	0.0545 ± 0.0012	0.01915 ± 0.00045	2190	34200	567932	427406	364224	240919	101351	12611	19899	4598	1012	238	300	201	30.8	18	6.9	
21	16.17 ± 0.35	0.0543 ± 0.0012	0.01926 ± 0.00045	1804	28900	537975	443719	365302	243326	100608	13428	18693	4197	951	208	286	153	39.7	17	3.3	
22	16.08 ± 0.35	0.0543 ± 0.0012	0.01964 ± 0.00044	2380	38200	560338	448613	363621	249672	101554	12913	19497	5125	1065	222	308	167	21.1	16	9.3	
23	16.08 ± 0.37	0.0594 ± 0.0016	0.01886 ± 0.00044	1704	84000	562447	391517	327886	231947	97635	12487	16281	4019	951	246	284	215	68.0	30	40.7	
24	16.18 ± 0.39	0.0536 ± 0.0012	0.01938 ± 0.00045	1650	29500	541772	417618	359914	238731	97230	12647	18693	4529	911	246	315	188	31.2	19	11.0	
25	16.37 ± 0.39	0.0546 ± 0.0012	0.01876 ± 0.00045	1900	57800	564957	417618	337284	232604	94797	11634	16935	4030	894	217	295	148	79.4	12	3.7	
26	16.43 ± 0.38	0.0550 ± 0.0013	0.01922 ± 0.00044	1663	27800	566667	422512	360991	243545	97635	12700	17236	4488	963	249	288	184	56.3	8	14.6	
27	16.32 ± 0.39	0.0549 ± 0.0012	0.01934 ± 0.00046	2000	32900	575949	432300	354526	249453	100608	13250	19347	4958	1167	255	306	177	47.8	17	7.3	
28	16.35 ± 0.38	0.0538 ± 0.0011	0.01948 ± 0.00046	3680	28300	582700	445351	363147	264770	118243	15062	25025	6648	1553	383	443	213	45.7	25	16.7	
29	16.58 ± 0.35	0.0539 ± 0.0011	0.01908 ± 0.00044	3050	32100	551899	432300	365776	240044	118243	14512	24171	6427	1451	352	399	221	43.3	16	7.7	
30	16.27 ± 0.38	0.0546 ± 0.0012	0.01941 ± 0.00046	1822	27600	562447	440457	375000	260394	104054	13694	21156	5235	1102	240	332	191	30.4	24	16.7	
31	16.63 ± 0.40	0.0544 ± 0.0013	0.01874 ± 0.00045	1925	28200	570042	437194	350216	232604	99324	11281	18693	4432	992	211	288	196	51.8	18	3.3	
32	16.68 ± 0.42	0.0546 ± 0.0012	0.01915 ± 0.00047	2130	35500	542194	419250	371767	248359	102703	13144	18191	4834	986	243	291	168	47.8	21	0.0	
33	16.36 ± 0.37	0.0541 ± 0.0012	0.01936 ± 0.00047	2220	29500	565640	414356	369612	257987	100338	13197	20402	4709	1053	248	300	174	39.3	8	13.4	
34	16.42 ± 0.39	0.0544 ± 0.0012	0.01944 ± 0.00047	1950	30300	587342	407830	355603	255580	100000	12824	19648	4598	1041	253	289	166	21.9	16	18.3	
35	16.39 ± 0.41	0.0542 ± 0.0012	0.01944 ± 0.00050	2480	32400	562025	412724	367457	245514	113446	14725	24372	6427	1439	341	452	231	64.4	16	24.8	
36	16.31 ± 0.36	0.0544 ± 0.0013	0.01912 ± 0.00041	2010	43900	580591	402936	355603	258425	90405	10533	16935	4460	850	208	242	168	49.4	3	3.3	
37	16.34 ± 0.44	0.0552 ± 0.0013	0.01948 ± 0.00050	2200	42200	582700	435563	365302	247046	100811	13002	21809	5512	1150	239	285	179	33.2	35	9.3	
38	16.54 ± 0.38	0.0543 ± 0.0012	0.01913 ± 0.00049	2148	44200	571308	414356	363147	247194	92770	11829	18543	4645	1008	214	286	162	49.4	24	8.9	
39	16.39 ± 0.44	0.0550 ± 0.0014	0.01960 ± 0.00053	1419	32800	565823	443719	365302	249234	91014	11901	16935	4598	907	222	267	157	51.8	22	6.1	
40	16.44 ± 0.39	0.0542 ± 0.0013	0.01949 ± 0.00047	1930	31600	565640	424144	362543	257112	96757	12504	19598	4903	1175	256	326	203	45.3	17	20.7	
41	16.37 ± 0.38	0.0548 ± 0.0012	0.01928 ± 0.00048	1690	40600	562447	435563	387931	262363	85405	11332	18342	4571	1045	239	333	178	41.3	28	13.4	
42	16.56 ± 0.41	0.0544 ± 0.0013	0.01950 ± 0.00049	1655	34400	573418	420881	350216	243107	92095	12131	19246	4654	1037	231	321	164	27.9	12	0.0	
43	16.26 ± 0.37	0.0545 ± 0.0013	0.01927 ± 0.00044	2490	37200	569198	432300	383621	245952	88108	10728	18291	4211	915	204	266	164	21.5	16	13.8	
44	16.33 ± 0.40	0.0540 ± 0.0012	0.01942 ± 0.00047	2260	30300	568694	437194	376078	247396	95338	14369	19950	4737	1089	232	300	160	49.4	9	8.5	
45	16.22 ± 0.37	0.0542 ± 0.0013	0.01942 ± 0.00045	1600	44700	528662	414356	329741	239168	95338	14369	18945	4820	1057	245	326	183	11.7	23	0.0	
46	16.57 ± 0.41	0.0539 ± 0.0013	0.01907 ± 0.00049	1674	39800	538397	402936	328664	237199	85135	11812	18542	4681	1089	215	289	180	50.0	14	0.0	
47	16.44 ± 0.42	0.0535 ± 0.0012	0.01927 ± 0.00048	1920	30300	528692	417618	351293	243326	94054	12771	18593	5208	1089	262	311	185	190	34.4	14	8.1
48	16.39 ± 0.40	0.0533 ± 0.0012	0.01936 ± 0.00049	1789	31400	540928	446992	350216	240263	89189	12220	17538	4349	898	202	317	151	21.5	19	5.7	
49	16.21 ± 0.37	0.0553 ± 0.0013	0.01947 ± 0.00046	1810	35800	570464	430669	375000	262582	99459	12824	21859	5125	1264	283	308	190	24.7	8	2.4	

Table 2B_U-Th_Pb+REE Monazite_McD_S

Spot	$^{238}\text{U}/^{206}\text{Pb}$	$^{207}\text{Pb}/^{206}\text{Pb}$	$^{206}\text{Pb}/^{232}\text{Th}$	U (ppm)	Th (ppm)	La (ppm)	Ce (ppm)	Pr (ppm)	Nd (ppm)	Sm (ppm)	Eu (ppm)	Gd (ppm)	Tb (ppm)	Dy (ppm)	Y (ppm)	Ho (ppm)	Er (ppm)	Tm (ppm)	Yb (ppm)	Lu (ppm)
50	16.40 ± 0.37	0.0543 ± 0.0012	0.01944 ± 0.00045	2020	31600	561603	411093	340517	233479	92838	12131	19196	4598	1000	219	337	168	215	14	16.7
51	16.66 ± 0.40	0.0543 ± 0.0011	0.01944 ± 0.00047	4730	33200	523207	432300	303879	243545	110135	14512	25879	6759	1650	358	575	217	79.8	31	7.7
52	16.54 ± 0.40	0.0540 ± 0.00122	0.01953 ± 0.000469	1900	36500	565554	474715	359914	258425	11263.8	14547	21859	5963	1341	318	410	239	69.6	35.4	13.4
53	16.61 ± 0.42	0.0544 ± 0.00132	0.01891 ± 0.000502	1596	66200	545992	412398	295259	233260	84932.43	11758	18593	4391	1085	255	308	212	30.0	11.2	5.3
54	16.49 ± 0.39	0.0569 ± 0.00129	0.01916 ± 0.000475	1611	57800	542616	437194	352371	244201	100202.7	13499	20804	4931	1081	232	350	159	36.4	21.7	8.1
55	16.34 ± 0.48	0.0537 ± 0.00125	0.01950 ± 0.000545	1760	30200	581013	476346	371767	246827	84729.73	13357	19599	4377	1024	193	251	169	32.8	25.5	5.7
56	16.80 ± 0.40	0.0541 ± 0.00115	0.01912 ± 0.000446	2240	37600	536709	438825	335129	235449	94797.3	11758	16985	4177	996	204	288	164	40.9	28.6	8.1
57	16.49 ± 0.41	0.0540 ± 0.00113	0.01979 ± 0.000522	3610	30800	526160	461664	355603	247484	111621.6	13979	26533	6648	1602	318	447	240	51.0	49.7	18.3
58	16.33 ± 0.40	0.0544 ± 0.00121	0.01865 ± 0.000471	2110	39100	568354	464927	329741	240700	80000	11279	16030	3767	748	165	216	128	38.9	16.8	0.0
59	16.59 ± 0.38	0.0542 ± 0.0012	0.01946 ± 0.000442	3130	33400	556118	461664	344828	250985	93648.65	11863	19898	4873	976	222	271	173	42.9	13.0	19.5
60	16.59 ± 0.38	0.0540 ± 0.0012	0.01944 ± 0.000447	3270	30600	567511	450245	322198	245733	111283.8	13854	23819	5956	1524	323	445	236	36.4	16.8	19.5
61	16.55 ± 0.40	0.0537 ± 0.00124	0.01905 ± 0.00045	1860	69500	540928	433931	309267	224508	87702.7	12256	16683	3518	752	174	209	156	36.4	6.8	13.4
62	16.14 ± 0.40	0.0538 ± 0.00114	0.01945 ± 0.000517	3700	34000	579325	481240	346983	233260	114189.2	14760	25226	6288	1467	359	498	232	72.1	27.3	32.5
63	16.35 ± 0.38	0.0539 ± 0.00121	0.01971 ± 0.000462	2030	32300	562700	477977	342672	245733	94256.76	13464	18894	4343	967	227	255	166	38.9	36.6	8.9
64	16.45 ± 0.44	0.0584 ± 0.00135	0.01954 ± 0.000525	1700	32600	584388	461664	345905	228665	100000	12398	22010	5457	1248	287	397	194	44.9	22.4	14.2
65	16.39 ± 0.40	0.0588 ± 0.00132	0.01921 ± 0.000471	1476	33600	602532	453507	372845	246827	86648.65	12007	18794	4609	988	210	277	182	65.2	19.9	13.8
66	16.37 ± 0.41	0.0588 ± 0.00127	0.01931 ± 0.000483	1900	42200	518987	451876	314655	231072	82297.3	12575	16432	3449	833	164	212	144	8.9	17.4	0.0
67	16.36 ± 0.40	0.0541 ± 0.00114	0.01942 ± 0.000473	2520	30760	554008	451876	355603	263020	112702.7	15293	23266	5789	1362	313	401	203	46.6	21.7	19.1
68	16.58 ± 0.40	0.0536 ± 0.00114	0.01947 ± 0.000486	4360	30500	551055	445351	365302	253611	106891.9	12895	21959	5180	1167	253	342	175	54.3	10.6	2.8
69	16.48 ± 0.36	0.0544 ± 0.00126	0.01949 ± 0.000443	2458	38700	540506	474715	376078	270460	98175.68	12860	19598	4571	1020	230	319	166	40.5	14.3	13.0
70	16.53 ± 0.39	0.0532 ± 0.00121	0.01933 ± 0.00046	2109	32100	576371	450408	367457	266521	106081.1	13606	20251	4535	1053	232	317	178	28.3	21.7	0.0
71	16.45 ± 0.44	0.0542 ± 0.0013	0.01924 ± 0.00052	1890	47000	562447	438825	335129	252079	98310.81	12877	19246	4321	959	221	321	186	34.0	13.7	19.1
72	16.48 ± 0.42	0.0544 ± 0.00118	0.01953 ± 0.000499	1660	34700	563966	491028	385776	286433	96013.51	13819	19749	4488	1179	283	364	203	44.5	15.5	8.5
73	16.27 ± 0.40	0.0557 ± 0.00123	0.01927 ± 0.000501	1970	86900	597046	405057	315733	243107	80135.14	11545	15829	3399	813	159	214	136	31.6	16.1	11.8
74	16.18 ± 0.41	0.0540 ± 0.00127	0.01937 ± 0.000484	2270	37100	594937	442088	334052	248578	89054.05	12078	18492	3853	833	192	251	157	15.0	16.8	13.4
75	16.17 ± 0.38	0.0535 ± 0.00122	0.01985 ± 0.000459	2460	31100	580591	451876	365302	266740	116216.2	14174	23317	5668	1276	276	394	232	25.5	26.1	14.6
76	16.11 ± 0.38	0.0542 ± 0.00126	0.01946 ± 0.000452	1563	33400	562278	446982	348060	269147	104729.7	14121	20251	4479	984	219	271	175	22.3	9.3	8.9

Table 3_U-Th_Pb Zircon sorted by age

Spot	Location	U (ppm)	Th (ppm)	Th/U	$^{207}\text{Pb}/^{235}\text{U}$	2σ	$^{206}\text{Pb}/^{238}\text{U}$	2σ	$^{207}\text{Pb}/^{209}\text{Pb}$	2σ	ρ	$^{207}\text{Pb}/^{235}\text{U}$ Age (Ma)	2σ	$^{206}\text{Pb}/^{238}\text{U}$ Age (Ma)	2σ	$^{207}\text{Pb}/^{209}\text{Pb}$ Age (Ma)	2σ	Probability of concordance
3	Core	690	223	0.32	10.760	0.242	0.423	0.0093	0.184	0.004	-0.05	2502	9	2272	18	2691	6	0.91
72		495	22	0.04	10.230	0.273	0.421	0.0111	0.174	0.004	0.06	2455	16	2264	33	2596	6	0.92
82		280	136	0.48	9.840	0.281	0.403	0.0112	0.177	0.004	-0.36	2418	19	2183	36	2625	5	0.90
80		46	34	0.74	6.460	0.176	0.364	0.0095	0.128	0.003	-0.06	2039	17	1998	29	2065	8	0.98
40		62	40	0.64	6.390	0.182	0.358	0.0097	0.130	0.003	-0.31	2030	18	1974	31	2095	9	0.97
37		151	53	0.35	6.426	0.151	0.358	0.0082	0.131	0.003	-0.19	2035	11	1972	19	2107	7	0.97
44		100	109	1.09	6.100	0.193	0.356	0.0108	0.124	0.003	-0.14	1989	21	1960	38	2020	8	0.99
2	Rim	444	141	0.32	8.210	0.198	0.355	0.0082	0.168	0.003	-0.31	2256	12	1958	19	2542	4	0.87
5		70	102	1.47	5.854	0.150	0.342	0.0090	0.125	0.003	0.01	1957	15	1895	28	2035	9	0.97
28		878	74	0.08	7.890	0.218	0.334	0.0090	0.173	0.004	-0.07	2218	18	1858	30	2584	10	0.84
48		28	15	0.53	6.030	0.251	0.334	0.0137	0.130	0.003	-0.12	1976	32	1856	58	2098	15	0.94
32		101	49	0.49	5.867	0.153	0.333	0.0085	0.129	0.003	0.18	1956	14	1853	26	2080	10	0.95
18		49	19	0.38	5.977	0.155	0.321	0.0083	0.137	0.003	0.03	1975	16	1799	23	2184	12	0.91
4		677	299	0.44	5.659	0.146	0.316	0.0080	0.130	0.003	-0.30	1924	14	1767	24	2103	5	0.92
83		48	22	0.47	5.510	0.163	0.314	0.0093	0.127	0.003	0.10	1906	20	1762	34	2056	15	0.93
39		125	113	0.90	5.190	0.144	0.309	0.0082	0.122	0.003	-0.39	1849	17	1737	27	1987	9	0.94
49		403	115	0.29	6.840	0.196	0.307	0.0083	0.161	0.003	-0.10	2090	18	1732	29	2466	9	0.83
35		182	124	0.68	5.660	0.158	0.298	0.0078	0.138	0.003	-0.22	1924	17	1683	25	2204	13	0.87
51		304	97	0.32	5.366	0.145	0.297	0.0079	0.131	0.003	-0.13	1878	16	1676	26	2111	5	0.89
66		693	223	0.32	6.470	0.176	0.295	0.0079	0.158	0.003	-0.11	2041	17	1664	26	2433	5	0.82
21		587	251	0.43	5.019	0.124	0.294	0.0070	0.125	0.003	-0.25	1824	12	1663	19	2028	5	0.91
16		118	107	0.91	5.043	0.126	0.294	0.0071	0.125	0.003	-0.23	1826	13	1660	20	2032	9	0.91
65		407	6	0.02	4.481	0.111	0.270	0.0067	0.120	0.002	0.15	1730	11	1539	20	1956	5	0.89
1		52	36	0.70	4.496	0.129	0.266	0.0072	0.122	0.003	-0.26	1729	17	1524	24	1995	14	0.88
22		128	32	0.25	4.144	0.103	0.266	0.0065	0.115	0.002	-0.13	1663	12	1519	19	1881	10	0.91
24		166	71	0.43	4.140	0.154	0.260	0.0086	0.117	0.002	-0.72	1660	25	1490	35	1910	12	0.90
54		66	43	0.64	4.218	0.118	0.253	0.0070	0.121	0.003	-0.09	1677	16	1452	25	1975	13	0.87
81		80	47	0.59	4.091	0.115	0.246	0.0068	0.120	0.003	0.00	1652	16	1417	24	1960	12	0.86
23		71	51	0.71	4.060	0.162	0.244	0.0080	0.121	0.003	-0.50	1650	29	1406	33	1979	15	0.85
31		41	17	0.41	3.840	0.134	0.236	0.0072	0.118	0.003	-0.29	1600	23	1367	28	1931	16	0.85
38		48	27	0.56	2.564	0.088	0.214	0.0072	0.087	0.002	0.00	1289	20	1251	31	1372	20	0.97
58		463	39	0.08	3.354	0.099	0.210	0.0060	0.116	0.002	-0.39	1496	18	1228	23	1903	10	0.82
46		275	126	0.46	2.377	0.068	0.208	0.0059	0.082	0.002	-0.19	1235	15	1219	22	1252	8	0.99
50		321	114	0.35	3.216	0.091	0.205	0.0059	0.115	0.002	-0.13	1463	16	1202	23	1876	8	0.82
9		53	45	0.84	2.485	0.076	0.170	0.0049	0.106	0.002	0.04	1267	17	1011	20	1724	17	0.80
41		36	16	0.45	2.302	0.077	0.156	0.0052	0.107	0.003	0.07	1211	19	935	23	1754	23	0.77
45		65	29	0.45	2.113	0.072	0.153	0.0047	0.100	0.002	-0.17	1152	19	919	20	1620	18	0.80
30		270	29	0.11	1.994	0.083	0.146	0.0049	0.099	0.002	-0.73	1111	25	878	22	1607	20	0.79
78		157	40	0.26	1.241	0.040	0.111	0.0031	0.081	0.002	-0.30	818	14	677	13	1215	19	0.83
77		397	18	0.05	1.284	0.042	0.111	0.0033	0.084	0.002	-0.40	838	15	675	14	1287	10	0.81
73		238	34	0.14	1.054	0.042	0.097	0.0028	0.077	0.002	-0.57	730	17	597	12	1121	24	0.82
19		224	185	0.83	0.775	0.020	0.096	0.0024	0.060	0.001	0.00	582	8	589	9	585	15	1.01
14		264	120	0.45	0.744	0.020	0.092	0.0024	0.059	0.001	0.06	564	8	567	10	564	18	1.00
69		39	33	0.84	0.687	0.022	0.089	0.0022	0.056	0.001	0.07	531	10	552	8	466	40	1.04
64		409	196	0.48	0.708	0.019	0.089	0.0021	0.058	0.001	0.02	544	8	549	7	531	15	1.01
56		37	66	1.77	0.693	0.026	0.089	0.0025	0.057	0.002	-0.24	534	13	548	10	494	49	1.02
52		113	49	0.44	0.720	0.022	0.088	0.0023	0.060	0.001	0.08	550	9	546	9	591	23	0.99
43		119	68	0.57	0.716	0.022	0.088	0.0025	0.059	0.001	-0.04	548	10	544	11	567	22	0.99
60	Core	148	95	0.64	0.708	0.019	0.087	0.0021	0.059	0.001	0.17	545	8	540	7	559	24	0.99
67		119	117	0.99	0.709	0.019	0.086	0.0024	0.059	0.001	0.20	544	7	532	10	574	24	0.98
52		456	176	0.39	0.691	0.018	0.086	0.0022	0.058	0.001	-0.01	535	8	538	8	539	12	1.00
27		61	45	0.74	0.681	0.023	0.086	0.0025	0.058	0.002	0.21	527	11	532	11	522	39	1.01
68		66	47	0.71	0.695	0.023	0.086	0.0023	0.058	0.001	0.04	535	11	531	9	558	33	0.99
42		136	114	0.84	0.692	0.020	0.086	0.0023	0.059	0.001	-0.12	534	9	530	9	551	24	0.99
13		184	64	0.35	0.674	0.017	0.085	0.0020	0.058	0.001	0.29	523	7	526	7	523	24	1.01
6		1215	931	0.77	0.694	0.016	0.085	0.0019	0.060	0.001	0.09	535	5	524	5	588	9	0.98
55		215	71	0.33	0.681	0.020	0.085	0.0021	0.058	0.001	-0.21	527	9	523	8	549	16	0.99
33		82	69	0.84	0.667	0.019	0.085	0.0025	0.058	0.001	0.10	519	9	523	10	512	26	1.01
12		74	55	0.75	0.656	0.018	0.084	0.0020	0.057	0.002	0.12	512	8	520	6	468	40	1.02
74	Core	48	38	0.78	0.675	0.021	0.084	0.0023	0.058	0.002	-0.04	524	10	519	9	520	42	0.99
34		296	229	0.77	0.655	0.017	0.083	0.0020	0.057	0.001	0.04	512	7	511	7	498	16	1.00
63		122	804	6.59	0.674	0.021	0.082	0.0022	0.059	0.001	-0.03	523	10	510	8	577	29	0.97
47		173	2	0.01	0.637	0.018	0.081	0.0019	0.058	0.001	-0.03	500	8	502	6	522	27	1.00
61	Rim	166	25	0.15	0.636	0.016	0.081	0.0020	0.057	0.001	0.25	500	6	502	7	481	18	1.00
7		763	40	0.05	0.761	0.021	0.080	0.0021	0.069	0.001	-0.49	575	8	497	8	903	13	0.86
67		394	4	0.01	0.635	0.015	0.079	0.0018	0.057	0.001	-0.15	499	5	493	6	500	14	0.99
75	Rim	222	5	0.02	0.625	0.017	0.079	0.0021	0.056	0.001	0.14	493	8	492	8	453	22	1.00
11		601	358	0.60	0.615	0.016	0.078	0.0020	0.057	0.001	0.02	487	6	486	7	501	13	1.00
26		125	103	0.82	0.604	0.015	0.078	0.0022	0.057	0.001	0.46	480	5	486	9	488	24	1.01
71		301	7	0.02	0.602	0.016	0.078	0.0020	0.056	0.001	0.18	478	6	482	7	453	19	1.01
21		261	11	0.04	0.685	0.082	0.077	0.0038	0.065	0.005	-0.90	524	46	479	21	740	140	0.90
10		393	91	0.23	0.582	0.016	0.075	0.0021	0.056	0.001	-0.13	465	7	468	8	463	14	1.00
53		253	8	0.03	0.581	0.017	0.075	0.0021	0.057	0.001	0.							

Table 4A_REE Zircon_McD_S sorted by age

Spot	U (ppm)	Th (ppm)	Pr (ppm)	Ce (ppm)	Nd (ppm)	Sm (ppm)	Eu (ppm)	Gd (ppm)	Tb (ppm)	Dy (ppm)	Ho (ppm)	Er (ppm)	Tm (ppm)	Yb (ppm)	Lu (ppm)	Th/U	Yb/Gd	Eu/Eu*	Ce/Sm	Lu/Dy	U/Ce	
8	937	352	29.04	0.13	3.49	9.41	45.27	22.38	337	609	1451	2381	3575	4818	5639	6870	0.38	29.63	0.18	2.66	0.47	53
36	1837	213	191262	97.47	360.99	678.34	1304.05	710.48	980	590	691	934	1188	1866	2845	4106	0.12	0.61	0.63	0.75	0.59	13
15	30	113786	0.04	3.33	0.67	3.06	17.91	8.35	56	47	46	39	29	26	35	34	0.13	0.71	0.26	0.77	0.07	110
59	989	54	115728	0.38	3.60	8.71	46.49	57.19	126	128	115	83	79	62	56	52	0.05	0.74	0.75	0.63	0.05	230
25	325	23	117864	0.04	2.64	0.48	11.35	7.99	32	36	46	60	84	155	213	309	0.07	4.06	0.42	0.96	0.67	200
76	223	27	121088	0.03	2.95	0.91	2.74	15.81	14.39	38	51	57	49	54	69	86	0.12	1.63	0.59	0.77	0.19	123
79	272	15	114466	0.05	0.86	0.68	7.84	6.04	40	142	277	330	292	231	177	170	0.06	2.89	0.34	0.46	0.06	514
20	258	17	118447	0.02	2.20	0.60	9.59	6.75	43	75	142	258	375	607	807	935	0.06	40.48	0.33	0.95	0.66	191
17	337	12	126214	0.06	1.89	0.52	1.53	6.22	4.97	74	208	383	625	1263	1870	2439	0.03	29.29	0.29	1.26	1.17	291
70	378	7	126117	0.08	1.45	0.10	0.96	3.91	27	111	271	463	689	927	1093	1179	0.02	17.14	0.33	1.19	0.44	425
53	253	8	123981	0.09	1.22	0.18	0.59	4.19	3.55	99	235	372	541	644	652	626	0.03	13.00	0.29	1.21	0.27	338
10	393	91	104563	0.03	57.59	0.64	2.12	9.05	6.75	66	122	283	504	813	1316	1764	0.23	17.39	0.28	26.34	0.88	11
29	261	11	116505	0.05	3.13	0.27	0.81	3.38	3.20	72	179	295	488	785	1075	1488	0.04	40.00	0.31	3.84	0.83	136
71	301	7	123204	0.13	2.76	1.83	4.16	7.64	4.44	35	136	326	582	938	1433	1820	0.02	27.14	0.27	1.50	0.70	178
26	125	103	94660	0.13	21.86	2.38	5.86	41.08	29.66	146	227	393	625	901	1239	1553	0.82	6.39	0.38	2.20	0.50	9
11	601	358	131456	0.05	36.87	1.93	4.60	36.89	23.09	143	211	427	647	1019	1615	2373	0.60	4.89	0.32	4.14	0.75	27
7	763	40	131553	0.87	9.15	10.13	11.36	28.78	28.60	165	404	661	1075	1822	2658	3374	0.05	9.80	0.52	1.32	0.83	136
67	394	4	122330	0.05	0.46	0.50	1.86	7.50	1.60	199	313	348	369	340	314	350	0.01	15.00	0.08	0.25	0.11	1407
75	222	5	119417	0.26	1.11	1.01	1.77	7.09	4.44	48	157	299	366	412	413	360	0.02	7.65	0.24	0.65	0.14	326
47	173	2	120291	0.05	0.17	0.05	0.42	5.20	3.02	43	124	247	229	193	186	182	0.01	8.67	0.20	0.14	0.08	1619
61	166	25	100291	0.05	12.07	0.44	1.31	10.07	7.46	106	241	366	534	806	1118	1398	0.15	5.52	0.35	4.97	0.58	22
63	122	804	22524	0.74	64.11	20.58	62.36	185.81	467.14	553	861	1363	1688	2126	2193	2309	0.77	24.81	0.23	25.07	0.75	4
34	296	229	109515	0.06	112.07	0.55	2.19	18.51	10.48	116	249	524	1007	1506	2324	2969	0.34	9.09	0.79	8.05	0.79	5
74	48	38	92427	0.08	14.71	0.56	1.53	7.57	16.16	56	121	267	445	749	1255	1503	0.78	7.50	0.30	4.05	0.64	6
12	74	55	84175	0.05	19.90	1.48	3.63	20.34	11.90	75	112	241	443	608	915	1286	0.75	12.92	0.34	4.68	0.70	21
55	215	71	99515	0.04	16.66	0.60	175.05	14.73	10.83	67	152	303	496	875	1215	1553	0.33	12.92	0.34	4.68	0.70	21
6	1215	931	83863	0.33	85.32	22.41	34.14	175.00	78.51	1127	2130	3205	4256	5980	7205	8699	0.77	12.47	0.21	2.02	0.41	23
33	82	69	77184	0.13	57.10	2.70	10.09	53.31	79.40	234	335	1081	1769	2725	3534	4634	0.84	7.16	0.71	4.44	0.65	2
13	184	64	96602	0.01	14.68	0.51	1.20	11.08	8.88	72	122	262	467	719	1053	1360	0.35	10.56	0.31	5.49	0.73	20
42	136	114	70291	0.15	26.59	3.59	14.22	44.26	58.97	157	235	382	641	950	1547	2000	0.84	6.67	0.71	2.49	0.69	8
68	66	47	93981	0.07	23.00	2.41	8.65	11.55	8.42	97	172	262	478	652	842	1224	0.71	4.69	0.63	11.02	0.71	5
57	119	117	74175	0.11	33.77	4.64	21.88	97.30	22.02	615	1085	1676	2350	2862	3385	3817	0.99	23.91	0.12	1.44	0.35	6
27	61	45	90097	0.01	21.40	0.59	2.67	10.47	8.70	71	103	213	352	523	814	1056	0.74	6.25	0.32	8.46	0.66	5
62	456	176	98068	0.05	21.70	2.33	7.26	38.45	30.02	202	365	588	962	1421	2087	2907	0.39	4.62	0.47	2.34	0.80	34
60	148	95	93107	0.12	31.32	4.38	13.37	50.68	41.03	130	248	442	617	906	1360	1646	0.64	6.22	0.51	2.56	0.49	8
43	119	68	84466	0.05	11.00	0.75	3.94	22.77	27.18	77	152	326	496	773	1202	1559	0.57	6.25	0.65	2.00	0.63	18
52	113	49	110874	0.02	36.87	0.55	2.10	15.68	16.16	95	217	480	830	1400	2117	2944	0.44	9.09	0.42	9.74	0.84	5
56	37	66	90971	0.09	118.60	1.95	7.07	49.66	27.53	402	793	1201	1756	2275	2522	3256	1.77	13.41	0.25	9.89	0.41	1
64	409	196	122196	0.05	45.35	0.86	3.41	20.27	1.78	101	224	480	835	1513	2275	2783	0.48	30.00	0.04	9.27	0.76	15
69	39	33	100583	0.01	19.90	0.66	1.82	12.16	14.03	57	124	226	374	623	834	1118	0.84	5.25	0.53	6.78	0.69	3
14	264	120	108835	0.01	27.08	1.31	2.47	11.35	3.91	72	116	253	449	688	1113	1404	0.45	13.85	0.14	9.88	0.77	16
73	238	34	114369	0.09	10.28	1.86	4.97	21.62	15.81	75	189	289	447	575	810	901	0.14	6.36	0.39	1.97	0.40	38

Table 4B_REE Zircon_McD_S sorted by age

Spot	Description	U (ppm)	Th (ppm)	Hf (ppm)	La (ppm)	Ce (ppm)	Pr (ppm)	Nd (ppm)	Sm (ppm)	Eu (ppm)	Gd (ppm)	Tb (ppm)	Dy (ppm)	Ho (ppm)	Er (ppm)	Tm (ppm)	Yb (ppm)	Lu (ppm)	Th/U	Yb/Gd	Eu/Eu*	Ce/Sm	Lu/Dy	U/Ce
19	o	224	185	100388	0.02	38.34	1.07	3.89	27.91	9.77	136	252	569	1004	1563	2413	3019	3813	0.63	34.50	0.16	5.69	0.67	10
77	m	397	18	123301	0.38	3.07	1.47	3.00	19.12	12.43	74	158	205	203	248	331	400	423	0.05	2.48	0.33	0.66	0.21	211
78	r	157	40	85631	0.18	11.75	1.50	1.95	6.01	11.19	28	53	89	121	238	416	573	907	0.26	3.62	0.86	8.09	1.02	22
30	r(o)	270	29	11068	0.04	4.26	0.24	0.94	6.15	6.22	55	120	256	410	628	955	1137	1402	0.11	13.53	0.34	2.87	0.55	103
45	c(s)	65	29	100971	0.05	7.94	0.17	1.05	9.32	8.35	26	66	132	194	333	474	609	793	0.45	6.19	0.54	3.53	0.60	13
41	c(h)	36	16	94660	0.03	15.01	0.44	1.55	7.09	9.77	47	71	138	225	406	619	814	1061	0.45	8.64	0.53	8.76	0.77	4
9	o	53	45	82718	0.03	35.73	1.76	4.99	21.35	13.68	101	129	269	434	559	789	1106	1358	0.84	7.62	0.30	6.93	0.50	2
50	c(o)	321	114	97087	0.38	18.76	0.80	3.74	14.46	18.29	59	108	226	379	621	976	1205	1565	0.35	8.21	0.62	5.37	0.69	28
58	c(o)	463	39	113010	0.30	4.32	1.37	2.47	15.54	14.92	59	124	200	273	375	502	632	850	0.08	2.94	0.49	1.15	0.43	175
46	c(h)	275	126	106825	0.03	41.60	0.69	3.44	25.34	3.37	137	260	488	766	1288	1753	2112	2817	0.46	10.87	0.20	6.80	0.58	11
38	c(o)	48	27	84078	0.05	13.51	1.23	4.46	22.50	9.59	107	174	341	549	869	1150	1547	2033	0.56	10.87	0.20	2.49	0.60	6
31	m	41	17	108350	0.04	15.50	0.22	0.83	6.08	4.97	13	29	51	104	181	307	492	720	0.41	6.40	0.57	10.56	1.40	4
22	c(h)	128	32	95728	0.01	1.75	0.68	2.52	9.59	1.15	26	199	23	54	102	136	167	199	0.25	8.14	0.07	0.75	0.37	119
24	c(h)	166	71	117573	0.02	6.04	1.00	3.04	17.91	4.97	86	94	126	132	143	153	151	157	0.43	2.56	0.13	1.40	0.12	45
65	c(s)	407	6	124078	0.02	0.44	0.29	0.88	13.58	2.13	89	216	261	218	201	213	239	239	0.02	3.55	0.06	0.13	0.09	1508
81	c(o)	80	47	79709	0.08	24.96	0.89	2.54	12.97	32.68	65	158	296	542	1025	1615	2348	3687	0.59	5.96	1.12	7.97	1.25	5
23	c(o)	71	51	90291	0.03	28.71	1.33	3.92	19.26	15.45	84	120	221	368	566	818	1236	1602	0.71	6.92	0.38	6.18	0.72	4
54	m	66	43	97379	0.31	22.51	0.82	3.79	16.28	10.48	76	125	205	344	533	794	981	1329	0.64	5.45	0.30	5.73	0.65	5
39	c(o)	125	113	92039	0.08	61.34	0.46	4.16	15.95	18.83	75	134	259	408	631	866	1261	1565	0.90	6.67	0.54	15.93	0.60	3
1	c(s)	52	36	89126	22.83	74.39	75.75	64.05	50.00	16.87	84	97	213	346	534	798	1186	1602	0.70	6.25	0.26	6.16	0.75	1
44	c(o)	100	109	83786	0.17	44.05	1.35	6.46	32.43	27.18	125	182	351	526	813	1097	1385	1772	1.09	5.43	0.43	5.63	0.50	4
21	o	587	251	110194	0.04	20.39	0.71	1.88	9.59	5.51	54	96	198	379	609	1000	1311	1748	0.43	10.40	0.24	8.80	0.88	47
16	c(o)	118	107	98835	8.02	83.20	86.21	78.77	76.35	27.89	118	124	251	425	650	1016	1478	2028	0.91	4.09	0.29	4.51	0.81	2
5	m	70	102	97767	0.01	25.61	0.58	1.33	5.81	4.80	36	60	136	222	373	595	786	1183	1.47	9.33	0.33	18.26	0.87	4
83	c(s)	48	22	81942	0.02	8.65	0.32	0.77	4.80	5.15	14	28	41	86	168	232	370	549	0.47	4.41	0.62	7.46	1.32	9
80	c(s)	46	34	98738	0.04	30.67	0.41	1.47	9.66	8.70	46	85	150	256	424	725	888	1240	0.74	7.08	0.41	13.15	0.83	2
32	o	101	49	103010	0.27	49.92	0.69	3.15	10.07	7.28	36	71	123	229	406	704	1075	1488	0.49	13.75	0.38	20.54	1.21	3
40	m(s)	62	40	89709	0.02	34.26	0.56	2.04	12.84	13.85	64	94	185	302	483	704	1025	1329	0.64	3.87	0.48	11.05	0.72	3
48	c(s)	28	15	91553	0.03	13.88	0.53	1.09	3.45	6.04	21	35	74	100	194	285	395	522	0.53	3.15	0.72	16.69	0.86	3
4	c(h)	677	299	110194	0.01	21.04	0.66	1.40	9.59	4.80	72	140	327	579	1025	1595	2329	3443	0.44	32.31	0.18	9.08	1.05	52
37	c(s)	151	53	94951	0.01	22.02	0.64	1.68	13.85	6.22	87	170	343	661	1150	1947	2391	3610	0.35	13.85	0.18	6.59	1.05	11
51	c(o)	304	97	107767	0.21	6.82	0.72	2.76	16.96	3.91	71	145	273	480	800	1089	1509	2167	0.32	17.65	0.11	1.67	0.79	73
18	c(o)	49	19	91553	0.05	10.77	0.73	1.01	9.12	5.51	42	80	186	344	500	846	1081	1439	0.38	17.33	0.28	4.89	0.77	7
35	o	182	124	99515	0.08	3.38	0.53	2.54	13.31	4.09	68	98	170	260	328	478	679	1000	0.68	10.00	0.14	1.05	0.40	88
66	c(o)	693	223	106699	0.23	16.97	1.29	4.75	17.16	44.23	59	116	204	352	580	781	1081	1411	0.32	2.17	1.39	4.09	0.69	67
49	c(o)	403	115	125922	0.11	2.28	0.54	2.01	20.07	1.74	93	161	232	251	306	348	337	386	0.29	11.58	0.04	0.47	0.17	288
2	r	444	141	105728	0.09	8.40	1.38	2.54	15.68	7.82	118	129	267	425	611	899	1118	1610	0.32	8.18	0.21	2.22	0.60	86
28	c(h)	878	74	98350	0.48	11.97	4.04	6.48	16.82	8.88	35	61	97	171	259	445	646	878	0.08	7.78	0.37	2.95	0.90	120
72	r	495	22	110194	0.03	7.26	0.39	0.61	4.73	3.37	34	65	145	229	432	700	994	1504	0.04	16.92	0.27	6.36	1.04	111
82	c(b)	280	136	129029	0.07	3.54	0.82	3.22	22.16	2.49	76	151	215	242	269	308	269	250	0.48	9.17	0.06	0.63	0.12	137
3	c(h)	690	223	96505	0.10	12.72	2.78	7.72	48.58	15.28	233	280	577	837	1231	1846	2304	2959	0.32	10.91	0.14	1.08	0.51	88